Defence Technology 18 (2022) 490–508

Contents lists available at ScienceDirect

Defence Technology

journal homepage: www.keaipublishing.com/en/journals/defence-technology

Finite element analysis of functionally graded sandwich plates with porosity via a new hyperbolic shear deformation theory

Pham Van Vinh [a, *], Le Quang Huy [b]

[a] Department of Solid Mechanics, Le Quy Don Technical University, 236 Hoang Quoc Viet, Hanoi, Viet Nam
[b] Institute of Techniques for Special Engineering, Le Quy Don Technical University, 236 Hoang Quoc Viet, Hanoi, Viet Nam

ARTICLE INFO

Article history:
Received 6 January 2021
Received in revised form
1 February 2021
Accepted 4 March 2021
Available online 9 March 2021

Keywords:
Functionally graded sandwich plates
Porous plates
Hyperbolic shear deformation theory
Bending analysis
Free vibration analysis
Buckling analysis

ABSTRACT

This study focusses on establishing the finite element model based on a new hyperbolic sheareformation theory to investigate the static bending, free vibration, and buckling of the functionally graded sandwich plates with porosity. The novel sandwich plate consists of one homogenous ceramic core and two different functionally graded face sheets which can be widely applied in many fields of engineering and defence technology. The discrete governing equations of motion are carried out via Hamilton's principle and finite element method. The computation program is coded in MATLAB software and used to study the mechanical behavior of the functionally graded sandwich plate with porosity. The present finite element algorithm can be employed to study the plates with arbitrary shape and boundary conditions. The obtained results are compared with available results in the literature to confirm the reliability of the present algorithm. Also, a comprehensive investigation of the effects of several parameters on the bending, free vibration, and buckling response of functionally graded sandwich plates is presented. The numerical results shows that the distribution of porosity plays significant role on the mechanical behavior of the functionally graded sandwich plates.

1. Introduction

In many fields of engineering and industry, traditional materials such as wood and metal are widely used for a long time ago. However, the mechanical properties of these materials do not meet the special requirements in many fields such as aerospace engineering, submarine engineering, defence engineering and nuclear power plant. In 1984, a group of material scientists in Japan proposed the functionally graded materials (FGMs) which are mixtures of two or more individual ingredients with a smooth and continuous varying of volume fractions and mechanical properties through the thickness of the plates and beams [1]. After that, the application of these materials is increased quickly. Therefore, a lot of scientists paid their attention to investigate the mechanical and thermal behaviors of these structures [2–6].

On the other hand, FGMs have been applied to multi-layered structures such as laminated or sandwich structures because of the gradual variation of the material properties at the interfaces between the face layers. These structures are usually used in high-temperature environments [7], so it is necessary to have an excellent understanding of the static and dynamic response of these structures. Nguyen et al. [8] applied first-order shear deformation theory (FSDT) to analyze the vibration and buckling behavior of functionally graded sandwich plates (FGSPs), in which a new improvement of the transverse shear stiffness has been employed to improve the accuracy and efficiency of FSDT. Nguyen et al. [9] developed a new refined simple FSDT for static bending and free vibration analysis of advanced composite plates. Thai et al. [10] analyzed the mechanical behavior of FGSP via a new FSDT, where the transverse displacement was divided into bending and shear parts. Also, it has been applied to analyze the static bending behavior of FGSP by Mantari et al. [11]. However, the shear stress of the FSDT does not equal to zeros at the surface of the plates, so it needs a shear correction factor which depends on the material, geometry as well as boundary conditions (BCs), so it is difficult to predict the exact value of the shear correction factor. It has prompted scientists to develop new theories that are more suitable to analyze beams, plates and shells. Zenkour [12,13] developed

* Corresponding author.
E-mail address: phamvanvinh@lqdtu.edu.vn (P. Van Vinh).
Peer review under responsibility of China Ordnance Society

https://doi.org/10.1016/j.dt.2021.03.006

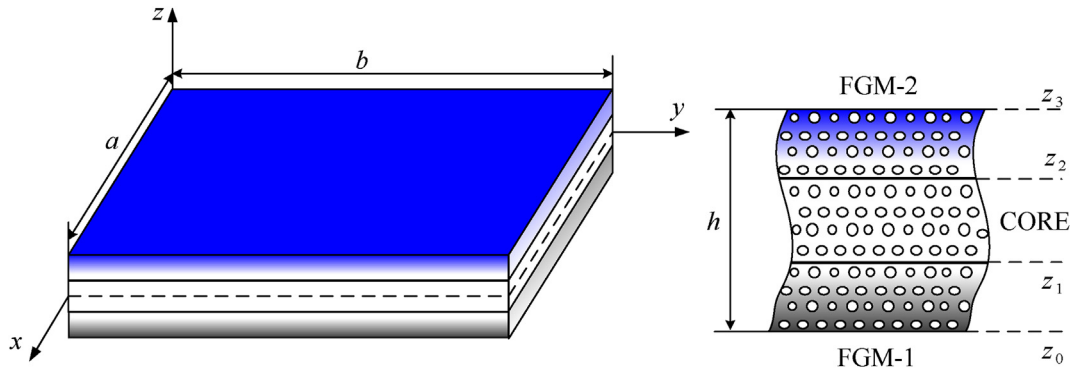

Fig. 1. The geometry and structure of the functionally graded sandwich plate with porosity.

third-order shear deformation theory (TSDT) and sinusoidal shear deformation theory (SSDT) to investigate the deflections, stresses, free vibration and buckling behavior of FGSPs. Tounsi and his co-workers [14–20] developed many simple and efficient HSDTs with non-polynomial shape functions to study the static and dynamic response of FGSPs. Vinh et al. [21,22] modified single variable shear deformation theory for static bending and free vibration analysis of FGM plates and FGM nanoplates. The thermomechanical bending of FGSP has been investigated by Li et al. [23] using a four-variable refined plate theory. In the work [24], Nguyen et al. developed a new HSDT with inverse trigonometric shape function to research the bending, free vibration and buckling of FGSP. Daikh [25,26] used HSDT with fifth-order polynomial shape function to investigate the effects of porosity on the bending, free vibration and buckling behavior of power-law and sigmoid FGSPs. Daikh et al. [27] used a hyperbolic shear deformation theory to analyze the static bending of multilayer nonlocal strain gradient nanobeams reenforced by carbon nanotubes. Sobhy [28] developed a four-variable shear deformation theory for hygro-thermal buckling of porous FGM sandwich microplates and microbeams. Taj et al. [29] analyzed the FG skew sandwich plates using HSDT in combination with finite element method (FEM). Xuan et al. [30] used isogeometric finite element analysis (IGA) based HSDT to analyze composite sandwich plates. Although the HSDT satisfies the stress-free conditions at two surfaces of the plates and does not need any shear correction factors, these theories neglect the effects of the thickness stretching on the behaviors of FGSPs, which are very important in the cases of thick plates.

To take into account the thickness stretching effects on the thick plates, various quasi-3D theories have been developed. Daikh et al. [31] established a quasi-3D theory in combination with nonlocal strain gradient for bending analysis of sigmoid FG sandwich nanoplates. Neves et al. [32,33] developed quasi-3D theories to investigate the static and dynamic response of the FGSP using the meshless method and radial basis functions method. Sobhy et al. [34] established a new quasi-3D theory to analyze free vibration and buckling behavior of the FGM nanoplates. Akavci [35] developed a new HSDT and quasi-3D theory to study the behavior of FGSP resting on elastic foundations. Bessaim et al. [36] established a new HSDT and normal (quasi-3D) deformation theory to research the bending and free vibration of FGSP with isotropic face sheets. The bending analysis of FGSP had been investigated by Zenkour [37] via a simple four-unknown shear and normal deformation (quasi-3D) theory. Furthermore, the FSDT and HSDT have been modified to Zig-Zag theory to study FGSP by Iurlaro et al. [38], Neves et al. [39], Dorduncu [40] and Garg et al. [41] to analyze the static and dynamic behavior of FGSPs. Liu et al. [42] used IGA in cooperation with higher-order layer-wise theory to analyze laminated composite and FG sandwich plates. Pandey et al. [43] used the layer-wise theory to analyze the free vibration of FGSP in the thermal environment. Burlayenko et al. [44] used three-dimensional finite elements to investigate the static bending and free vibration behavior of the FGSP with the material properties are calculated via Mori-Tanaka homogenization method.

The use of FGSPs in the fact shows that these structures usually contact to different loads and environments such as static loads, dynamic loads, blast loads and high-temperature environments [45]. On the other hand, porosity is usually appeared in materials during the fabrication process or intentionally created. By including porosity, the stiffness of the structures is reduced, but it also reduces the mass of the structures. Besides, the optimization of the material distribution, as well as the porous distribution through the thickness of these structures, can improve the strength of the structures or avoid the stress concentration phenomenon at the surfaces. So, the sandwich structures can be made of many different types of FGM layers to maintain these features. Hence, FGSP with porosity has been widely applied in many fields of engineering including defence technology. For example, the FGSP with porosity can be used to make the tank armor that can withstand nuclear explosions. The cover of military aircraft or special military equipment can be made from FGSP with porosity to reduce their weight. Besides, the outer skin and fuel tanks of missiles are made of special FGSP with porosity to reduce the total weight and increase heat resistance. A lot of scientists have been focused on the investigation of the static and dynamic response of the isotropic and sandwich FG plates with porosity. Shahsavari et al. [46] developed a new quasi-3D hyperbolic theory for free vibration of FG plates with porosities resting on elastic foundations. Zenkour [47] analyzed the mechanical behavior of FG single-layered and sandwich plates with porosities. Barati et al. [48,49] analyzed vibration and post-buckling of porous graphene platelet reinforced beams and cylindrical shells with different porosity distributions. Sobhy et al. [50] considered the effects of porosity on the buckling and vibration of double-FGM nanoplates via a quasi-3D refined theory. Zenkour et al. [51] studied the effects of porosity on the thermal buckling behavior of actuated FG piezoelectric nanoplates. The displacement and stresses of FG porous plates are investigated by Zenkour [52] via a quasi-3D refined theory. Mashat et al. [53] developed a new quasi-3D higher-order plate theory for bending analysis of porous FG plates resting on elastic foundations under hygro-thermo-mechanical loads.

In this study, a novel functionally graded sandwich plate (FGSP) with three types of porous distribution is introduced and investigated with static bending, free vibration and buckling problems. The outlines of the paper are as follows: the basic formulation of the problem is given in section 2, including the construction of

FGSP with three types of porosity, the formulation of the new hyperbolic shear deformation theory and finite element formulations. Section 3 gives the convergency and verification study as well as the benchmark numerical results of the static bending, free vibration and buckling behavior of the FGSP with porosity with many useful discussions in each subsection. Section 4 gives some important summaries and good ideas for future works on the investigation of these structures.

2. Problem formulation

2.1. Functionally graded sandwich plates with porosity

The mechanical behaviors of a novel sandwich plate with porosity are investigated in this study. The sandwich plate consists of one homogenous ceramic core and two different functionally graded face sheets. The dimension of the sandwich plates is a in x-direction, b in y-direction and the total thickness is h as shown in Fig. 1. A group of three numbers as "$i-j-k$" is used to denote the ratio of the thicknesses of the bottom-core-top layers. It means the thickness of the bottom layer is $h.i/(i+j+k)$, that of core layer is $h.j/(i+j+k)$ and that of top layer is $h.k/(i+j+k)$.

2.1.1. The FGSP model with even porous face sheets (porosity I)

The variation of the effective material properties through the thickness of the FGSP with porosity I are obtained by the following formulae

$$\begin{cases} P(z)=P_{\mathrm{b}}+(P_{\mathrm{c}}-P_{\mathrm{b}})\left(\dfrac{z-z_0}{z_1-z_0}\right)^p-\dfrac{\xi}{2}(P_{\mathrm{b}}+P_{\mathrm{c}}) & z_0\le z\le z_1 \\ P(z)=P_{\mathrm{c}} & z_1<z<z_2 \\ P(z)=P_{\mathrm{t}}+(P_{\mathrm{c}}-P_{\mathrm{t}})\left(\dfrac{z-z_3}{z_2-z_3}\right)^p-\dfrac{\xi}{2}(P_{\mathrm{t}}+P_{\mathrm{c}}) & z_2\le z\le z_3 \end{cases} \tag{1}$$

where P_{b}, P_{t} and P_{c} are the material properties of the materials at bottom surface, top surface and core layer of the sandwich plates, and ξ is the coefficient of porosity ($\xi \ll 1$).

2.1.2. The FGSP model with linear-uneven porous face sheets (porosity II)

For the FGSP with one perfect core and two linear-uneven porous face sheets, the effective material properties are calculated by the following formula

$$\begin{cases} P(z)=P_{\mathrm{b}}+(P_{\mathrm{c}}-P_{\mathrm{b}})\left(\dfrac{z-z_0}{z_1-z_0}\right)^p-\dfrac{\xi}{2}(P_{\mathrm{b}}+P_{\mathrm{c}})\left(1-\dfrac{z-z_0}{z_1-z_0}\right) & z_0\le z\le z_1 \\ P(z)=P_{\mathrm{c}} & z_1<z<z_2 \\ P(z)=P_{\mathrm{t}}+(P_{\mathrm{c}}-P_{\mathrm{t}})\left(\dfrac{z-z_3}{z_2-z_3}\right)^p-\dfrac{\xi}{2}(P_{\mathrm{t}}+P_{\mathrm{c}})\left(\dfrac{z-z_2}{z_3-z_2}\right) & z_2\le z\le z_3 \end{cases} \tag{2}$$

2.1.3. The FGSP model with linear-uneven porous core (porosity III)

The effective material properties of FGSP with one linear-uneven porous core and two perfect face sheets are described by the following formula

$$\begin{cases} P(z)=P_{\mathrm{b}}+(P_{\mathrm{c}}-P_{\mathrm{b}})\left(\dfrac{z-z_0}{z_1-z_0}\right)^p & z_0\le z\le z_1 \\ P(z)=P_{\mathrm{c}}-\xi P_{\mathrm{c}}\left(1-\dfrac{|2z-(z_2+z_1)|}{z_2-z_1}\right) & z_1<z<z_2 \\ P(z)=P_{\mathrm{t}}+(P_{\mathrm{c}}-P_{\mathrm{t}})\left(\dfrac{z-z_3}{z_2-z_3}\right)^p & z_2\le z\le z_3 \end{cases} \tag{3}$$

The perfect FGSP are obtained easily by setting the porous coefficient $\xi=0$ in Eqs. (1)–(3).

2.2. Finite element formulation

2.2.1. Displacement field and strains

The higher-order shear deformation theory is adopted in this study to describe the displacement of the sandwich plate as follows

$$\begin{cases} u(x,y,z,t)=u(x,y,t)+f(z)\beta^u(x,y,t)+g(z)\theta^u(x,y,t) \\ v(x,y,z,t)=v(x,y,t)+f(z)\beta^v(x,y,t)+g(z)\theta^v(x,y,t) \\ w(x,y,z,t)=w(x,y,t) \end{cases} \tag{4}$$

where u, v, w, β^u, β^v, θ^u, θ^v are seven unknown displacement functions at the middle surface of the plate and $f(z)$, $g(z)$ are the shape function. Numerous shape functions have been introduced in the literature. In this study, the novel hyperbolic shape functions of $f(z)$ and $g(z)$ are given as follows

$$\begin{aligned} f(z)&=\Omega.\tanh\left(\frac{z}{h}\right)+\Phi.\sinh\left(\frac{\pi z}{h}\right);\ g(z) \\ &=z-\Omega.\tanh\left(\frac{z}{h}\right)+\Phi.\sinh\left(\frac{\pi z}{h}\right) \end{aligned} \tag{5}$$

where

$$\begin{aligned} \Omega&=\frac{5h\cosh\left(\frac{\pi}{2}\right)}{4\left[\tanh^2\left(\frac{1}{2}\right)+\cosh\left(\frac{\pi}{2}\right)-1\right]};\ \Phi \\ &=\frac{5h\left[\tanh^2\left(\frac{1}{2}\right)-1\right]}{4\pi\left[\tanh^2\left(\frac{1}{2}\right)+\cosh\left(\frac{\pi}{2}\right)-1\right]} \end{aligned} \tag{6}$$

The strain fields of the plate are

$$\begin{aligned} \boldsymbol{\varepsilon}&=\boldsymbol{\varepsilon}^0+f\boldsymbol{\varepsilon}^1+g\boldsymbol{\varepsilon}^2 \\ \boldsymbol{\gamma}&=f'\boldsymbol{\gamma}_1+g'\boldsymbol{\gamma}_2 \end{aligned} \tag{7}$$

where

$$\boldsymbol{\varepsilon}^0 = \begin{Bmatrix} u_{,x} \\ v_{,y} \\ u_{,y} + v_{,x} \end{Bmatrix}, \quad \boldsymbol{\varepsilon}^1 = \begin{Bmatrix} \beta^u_{,x} \\ \beta^v_{,y} \\ \beta^u_{,y} + \beta^v_{,x} \end{Bmatrix}, \quad \boldsymbol{\varepsilon}^2 = \begin{Bmatrix} \theta^u_{,x} \\ \theta^v_{,y} \\ \theta^u_{,y} + \theta^v_{,x} \end{Bmatrix} \tag{8}$$

$$\gamma_1 = \begin{Bmatrix} \gamma^u_1 \\ \gamma^v_1 \end{Bmatrix} = \begin{Bmatrix} w_{,x} + \beta^u \\ w_{,y} + \beta^v \end{Bmatrix}, \ \gamma_2 = \begin{Bmatrix} \gamma^u_2 \\ \gamma^v_2 \end{Bmatrix} = \begin{Bmatrix} w_{,x} + \theta^u \\ w_{,y} + \theta^v \end{Bmatrix} \tag{9}$$

The lower comma is used to denote the derivation respect to the following variable. It can be seen that $f' = 0$ and $g' \neq 0$ at $z = \pm h/2$, so $\boldsymbol{\gamma}_2(\pm h/2)$ has to equal to zeros to satisfy the shear stress free conditions at the top and bottom surfaces of the plate. This condition of the shear strain will be treated at element level in finite element formulation later. As a consequence, the shear strain vector can be obtained via $\boldsymbol{\gamma}_1$ as follows

$$\gamma = \begin{Bmatrix} \gamma_{xz} \\ \gamma_{yz} \end{Bmatrix} = f' \begin{Bmatrix} \gamma^u_1 \\ \gamma^v_1 \end{Bmatrix} = f' \gamma_1 \tag{10}$$

2.2.2. Constitutive relations

The linear constitutive relations of the plates are

$$\boldsymbol{\sigma} = \boldsymbol{D}\boldsymbol{\varepsilon}, \quad \boldsymbol{\tau} = \boldsymbol{D}_s \boldsymbol{\gamma} \tag{11}$$

where

$$\boldsymbol{\sigma} = \{ \sigma_x \quad \sigma_y \quad \tau_{xy} \}^{\mathrm{T}}, \quad \boldsymbol{\tau} = \{ \tau_{xz} \quad \tau_{yz} \}^{\mathrm{T}} \tag{12}$$

$$\boldsymbol{D} = \begin{bmatrix} C_{11} & C_{12} & 0 \\ C_{12} & C_{22} & 0 \\ 0 & 0 & C_{66} \end{bmatrix}, \quad \boldsymbol{D}_s = \begin{bmatrix} C_{55} & 0 \\ 0 & C_{44} \end{bmatrix} \tag{13}$$

$$C_{11} = C_{22} = \frac{E(z)}{1-\nu^2}, \ C_{12} = \nu C_{11}, \ C_{44} = C_{55} = C_{66} = \frac{E(z)}{2(1+\nu)} \tag{14}$$

where $E(z)$, ν are Young's modulus and Poisson's ratio, respectively. It is noticed that the Poisson's ratio is assumed constant and equal to each material.

In this study, Hamilton's principle is adopted to obtain the equation of motion of the plates

$$0 = \int_0^T (\delta \Pi + \delta W + \delta V - \delta T) \mathrm{d}t \tag{15}$$

where $\delta\Pi$, $\delta W, \delta V$, δT are respectively the variations of strain energy, work done by external force, work done by in-plane compressive load and kinetic energy of the plate.

2.2.3. Strain energy

The expression of the variation of the strain energy is obtained as follows

$$\begin{aligned} \delta \Pi &= \frac{1}{2}\delta \int_V \left(\boldsymbol{\varepsilon}^{\mathrm{T}} . \boldsymbol{\sigma} + f' \boldsymbol{\gamma}_1{}^{\mathrm{T}} . \boldsymbol{\tau} \right) dV \\ &= \int_V \left\{ \left[\delta\boldsymbol{\varepsilon}^0 + f\delta\boldsymbol{\varepsilon}^1 + g\delta\boldsymbol{\varepsilon}^2 \right]^{\mathrm{T}} . \boldsymbol{D} \left(\boldsymbol{\varepsilon}^0 + f\boldsymbol{\varepsilon}^1 + g\boldsymbol{\varepsilon}^2 \right) + \delta\boldsymbol{\gamma}_1^{\mathrm{T}} . f' . \boldsymbol{\tau} \right\} \mathrm{d}V \end{aligned} \tag{16}$$

After rearranging into matrix form and integrating through the thickness of the plate, the variation of strain energy of the plate can be calculated as follows

$$\delta \Pi = \int_A \left(\delta\boldsymbol{\omega}^{\mathrm{T}} \boldsymbol{P} + \delta\boldsymbol{\gamma}_1^{\mathrm{T}} \boldsymbol{Q}_1 \right) \mathrm{d}A \tag{17}$$

where $\boldsymbol{R}$ and $\boldsymbol{T}_1$ are the vector of stress resultants which are given by

$$\boldsymbol{P} = \boldsymbol{H}\boldsymbol{\omega}, \quad \boldsymbol{Q}_1 = \boldsymbol{H}_s \boldsymbol{\gamma}_1, \quad \boldsymbol{\omega} = \{ \boldsymbol{\varepsilon}^{0\mathrm{T}} \quad \boldsymbol{\varepsilon}^{1\mathrm{T}} \quad \boldsymbol{\varepsilon}^{2\mathrm{T}} \}^{\mathrm{T}} \tag{18}$$

where

$$\boldsymbol{H} = \int_z \begin{bmatrix} \boldsymbol{D} & f\boldsymbol{D} & g\boldsymbol{D} \\ f\boldsymbol{D} & f^2\boldsymbol{D} & fg\boldsymbol{D} \\ g\boldsymbol{D} & fg\boldsymbol{D} & g^2\boldsymbol{D} \end{bmatrix} \mathrm{d}z, \quad \boldsymbol{H}_s = \int_z (f^{'})^2 \boldsymbol{D}_s \mathrm{d}z \tag{19}$$

2.2.4. Work done by external force

The variation of work done by external transverse load is obtained by

$$\delta W = \int_A q\delta w \mathrm{d}A \tag{20}$$

2.2.5. Work done by in-plane compressive loads

The variation of work done by in-plane compressive loads is calculated by

$$\delta V = \int_V \left(\boldsymbol{\sigma}^0 \right)^{\mathrm{T}} \delta\boldsymbol{\varepsilon}_{NL} \mathrm{d}V \tag{21}$$

where

$$\boldsymbol{\sigma}^0 = \left\{ \sigma_x^0 \quad \sigma_y^0 \quad \tau_{xy}^0 \right\}^{\mathrm{T}} \tag{22}$$

and the Von Karman nonlinear strains $\boldsymbol{\varepsilon}_{\mathrm{NL}}$ is expressed as

$$\boldsymbol{\varepsilon}_{\mathrm{NL}} = \frac{1}{2} \begin{bmatrix} \left(\frac{\partial u}{\partial x} \right)^2 + \left(\frac{\partial v}{\partial x} \right)^2 + \left(\frac{\partial w}{\partial x} \right)^2 \\ \left(\frac{\partial u}{\partial y} \right)^2 + \left(\frac{\partial v}{\partial y} \right)^2 + \left(\frac{\partial w}{\partial y} \right)^2 \\ 2\left(\frac{\partial u}{\partial x}\frac{\partial u}{\partial y} + \frac{\partial v}{\partial x}\frac{\partial v}{\partial y} + \frac{\partial w}{\partial x}\frac{\partial w}{\partial y} \right) \end{bmatrix} \tag{23}$$

By including the displacement field Eq. (4) into Eq. (23), the variation of work done by in-plane compressive loads is obtained as

$$\delta V = \int_S \left(\nabla \boldsymbol{q}^{\mathrm{T}} \boldsymbol{S}^0 \nabla \delta\boldsymbol{q} \right) \mathrm{d}S \tag{24}$$

where $.\nabla = \{\partial/\partial x, \ \partial/\partial y\}^{\mathrm{T}}.$, $\boldsymbol{q} = \{u, \ v, \ w\}^{\mathrm{T}}$. The matrix $\boldsymbol{S}^0$ are given by

$$\boldsymbol{S}^0 = \begin{bmatrix} \lambda^0 & \mathbf{0} & \mathbf{0} & \lambda^1 & \mathbf{0} & \lambda^2 & \mathbf{0} \\ \mathbf{0} & \lambda^0 & \mathbf{0} & \mathbf{0} & \lambda^1 & \mathbf{0} & \lambda^2 \\ \mathbf{0} & \mathbf{0} & \lambda^0 & \mathbf{0} & \mathbf{0} & \mathbf{0} & \mathbf{0} \\ \lambda^1 & \mathbf{0} & \mathbf{0} & \lambda^{11} & \mathbf{0} & \lambda^{12} & \mathbf{0} \\ \mathbf{0} & \lambda^1 & \mathbf{0} & \mathbf{0} & \lambda^{11} & \mathbf{0} & \lambda^{12} \\ \lambda^2 & \mathbf{0} & \mathbf{0} & \lambda^{12} & \mathbf{0} & \lambda^{22} & \mathbf{0} \\ \mathbf{0} & \lambda^2 & \mathbf{0} & \mathbf{0} & \lambda^{12} & \mathbf{0} & \lambda^{22} \end{bmatrix} \tag{25}$$

where

$$\lambda^0 = \int_h \widehat{\boldsymbol{\sigma}}^0 \mathrm{d}z,\ \lambda^1 = \int_h f\widehat{\boldsymbol{\sigma}}^0 \mathrm{d}z,\ \lambda^2 = \int_h g\widehat{\boldsymbol{\sigma}}^0 \mathrm{d}z,\ \lambda^{11} = \int_h f^2\widehat{\boldsymbol{\sigma}}^0 \mathrm{d}z,\ \lambda^{22} = \int_h g^2\widehat{\boldsymbol{\sigma}}^0 \mathrm{d}z,\ \lambda^{12} = \int_h fg\widehat{\boldsymbol{\sigma}}^0 \mathrm{d}z \tag{26}$$

$$\widehat{\boldsymbol{\sigma}}^0 = \begin{bmatrix} \sigma_x^0 & \tau_{xy}^0 \\ \tau_{xy}^0 & \sigma_y^0 \end{bmatrix} \tag{27}$$

2.2.6. Kinetic energy

The variation of the kinetic energy of the plate is obtained as

$$\delta T = \int_V \rho\left(\dot{u}\delta\dot{u} + \dot{v}\delta\dot{v} + \dot{w}\delta\dot{w}\right)\mathrm{d}V = \int_S \delta\dot{\boldsymbol{q}}^{\mathrm{T}}\boldsymbol{I}_0\dot{\boldsymbol{q}}\mathrm{d}S \tag{28}$$

where $\boldsymbol{I}_0$ are obtained as the following formulae

$$\boldsymbol{I}_0 = \int_h \boldsymbol{L}^{\mathrm{T}}\rho\boldsymbol{L}\mathrm{d}z,\ \ \boldsymbol{L} = \begin{bmatrix} 1 & 0 & 0 & f & 0 & g & 0 \\ 0 & 1 & 0 & 0 & f & 0 & g \\ 0 & 0 & 1 & 0 & 0 & 0 & 0 \end{bmatrix} \tag{29}$$

2.2.7. Finite element formulations

A four-node quadrilateral plate element with seven degrees of freedom is employed to investigate the FGSP with porosity. The nodal displacement vector of the $i-th$ node is

$$\boldsymbol{d}_i = \left\{ u_i \quad v_i \quad w_i \quad \beta_i^u \quad \beta_i^v \quad \theta_i^u \quad \theta_i^v \right\}^{\mathrm{T}},\ i = \overline{1,4} \tag{30}$$

The nodal displacement vector of the plate element, $\boldsymbol{U}_{\mathrm{e}}$, is defined as

$$\boldsymbol{U}_{\mathrm{e}} = \left\{ \boldsymbol{d}_1^{\mathrm{T}} \quad \boldsymbol{d}_2^{\mathrm{T}} \quad \boldsymbol{d}_3^{\mathrm{T}} \quad \boldsymbol{d}_4^{\mathrm{T}} \right\}^{\mathrm{T}} \tag{31}$$

The coordinates and displacement variables at any points of the element are approximated via the shape functions as following formulae

$$\begin{cases} x = \sum N_i x_i & y = \sum N_i y_i \\ u = \sum N_i u_i & v = \sum N_i v_i \\ w = \sum N_i w_i & \\ \beta^u = \sum N_i \beta_i^u & \beta^v = \sum N_i \beta_i^v \\ \theta^u = \sum N_i \theta_i^u + N_m \theta_m^u & \theta^v = \sum N_i \theta_i^v + N_m \theta_m^v \end{cases} \tag{32}$$

where N_i are the linear shape functions and N_m is a quadratic shape function which are given by

$$\begin{aligned} N_1 &= \frac{1}{4}(1-\xi)(1-\eta),\ \ N_2 = \frac{1}{4}(1+\xi)(1-\eta) \\ N_3 &= \frac{1}{4}(1+\xi)(1+\eta),\ \ N_4 = \frac{1}{4}(1-\xi)(1+\eta) \\ N_m &= \frac{1}{16}\left(1-\xi^2\right)\left(1-\eta^2\right) \end{aligned} \tag{33}$$

The coefficients $\theta_m^u,\ \theta_m^v$ are used to treat the condition $\gamma_2 = 0$ at the bottom and top surfaces of the plates, which is performed in the integral form as follows

$$\int_A \gamma_2 \mathrm{d}A = \int_A \begin{Bmatrix} w_{,x} + \theta^u \\ w_{,y} + \theta^v \end{Bmatrix} \mathrm{d}A = 0 \tag{34}$$

By substituting $w,\ \theta^u,\ \theta^v$ from (32) into (34), one gets

$$\int_A \begin{Bmatrix} \sum N_{i,x} w_i + \sum N_i \theta_i^u + N_m \theta_m^u \\ \sum N_{i,y} w_i + \sum N_i \theta_i^v + N_m \theta_m^v \end{Bmatrix} \mathrm{d}A = \mathbf{0} \tag{35}$$

From the expression of Eq. (35), the parameter θ_m^u and θ_m^v can be calculated by

$$\theta_m^u = \frac{-1}{\Psi}\left(t_1^u w_1 + t_2^u w_2 + t_3^u w_3 + t_4^u w_4 + c_1\theta_1^u + c_2\theta_2^u + c_3\theta_3^u + c_4\theta_4^u\right) \tag{36}$$

$$\theta_m^v = \frac{-1}{\Psi}\left(t_1^v w_1 + t_2^v w_2 + t_3^v w_3 + t_4^v w_4 + c_1\theta_1^v + c_2\theta_2^v + c_3\theta_3^v + c_4\theta_4^v\right) \tag{37}$$

In Eqs. (36) and (37), the parameters $t_i^u,\ t_i^v,\ c_i$ and Ψ are calculated as the following formulae

$$t_i^u = \int_A N_{i,x}\mathrm{d}A,\quad t_i^v = \int_A N_{i,y}\mathrm{d}A,\quad c_i = \int_A N_i \mathrm{d}A,\quad \Psi = \int_A N_m \mathrm{d}A,\ \ i = \overline{1,4} \tag{38}$$

Now Eqs. (36) and (37) can be rewritten in matrix form as follows

$$\theta_{\mathrm{m}}^{u}=\boldsymbol{B}_{\mathrm{f0}}^{u}\boldsymbol{U}_{\mathrm{e}},\quad \theta_{\mathrm{m}}^{v}=\boldsymbol{B}_{\mathrm{f0}}^{v}\boldsymbol{U}_{\mathrm{e}} \tag{39}$$

where

$$\begin{aligned}\boldsymbol{B}_{\mathrm{f0}}^{u}&=\frac{-1}{\Psi}\left[0\quad 0\quad t_1^{u}\quad 0\quad 0\quad c_1\quad 0\quad 0\quad 0\quad t_2^{u}\quad 0\quad 0\quad c_2\quad 0\,0\quad 0\quad t_3^{u}\quad 0\quad 0\quad c_3\quad 0\quad 0\quad 0\quad t_4^{u}\quad 0\quad 0\quad c_4\quad 0\right]\\ \boldsymbol{B}_{\mathrm{f0}}^{v}&=\frac{-1}{\Psi}\left[0\quad 0\quad t_1^{v}\quad 0\quad 0\quad 0\quad c_1\quad 0\quad 0\quad t_2^{v}\quad 0\quad 0\quad 0\quad c_2\,0\quad 0\quad t_3^{v}\quad 0\quad 0\quad 0\quad c_3\quad 0\quad 0\quad t_4^{v}\quad 0\quad 0\quad 0\quad c_4\right]\end{aligned} \tag{40}$$

Eq. (39) is inserted into Eq. (32), it leads to

$$\begin{aligned}\theta^{u}&=\sum N_i\theta_i^{u}+N_{\mathrm{m}}\theta_{\mathrm{m}}^{u}=\sum N_i\theta_i^{u}+N_{\mathrm{m}}\left(\boldsymbol{B}_{\mathrm{f0}}^{u}\right)\boldsymbol{U}_{\mathrm{e}}\\ \theta^{v}&=\sum N_i\theta_i^{v}+N_{\mathrm{m}}\theta_{\mathrm{m}}^{v}=\sum N_i\theta_i^{v}+N_{\mathrm{m}}\left(\boldsymbol{B}_{\mathrm{f0}}^{v}\right)\boldsymbol{U}_{\mathrm{e}}\end{aligned} \tag{41}$$

2.2.7.1Introducing Eq. (41) into expression of $\delta\varepsilon^2$, one gets

$$\begin{aligned}\delta\boldsymbol{\varepsilon}^2=&\begin{Bmatrix}\sum N_{i,x}\delta\theta_i^{u}\\ \sum N_{i,y}\delta\theta_i^{v}\\ \sum N_{i,y}\delta\theta_i^{u}+\sum N_{i,x}\delta\theta_i^{v}\end{Bmatrix}\\ &+\begin{Bmatrix}N_{\mathrm{m},x}\boldsymbol{B}_{\mathrm{f0}}^{u}\delta\boldsymbol{U}_{\mathrm{e}}\\ N_{\mathrm{m},y}\boldsymbol{B}_{\mathrm{f0}}^{v}\delta\boldsymbol{U}_{\mathrm{e}}\\ N_{\mathrm{m},y}\boldsymbol{B}_{\mathrm{f0}}^{u}\delta\boldsymbol{U}_{\mathrm{e}}+N_{\mathrm{m},x}\boldsymbol{B}_{\mathrm{f0}}^{v}\delta\boldsymbol{U}_{\mathrm{e}}\end{Bmatrix}\end{aligned} \tag{42}$$

The variation of the axial strain vector can be rewritten in short form as

$$\delta\boldsymbol{\omega}=\boldsymbol{B}\delta\boldsymbol{U}_{\mathrm{e}}=\left(\boldsymbol{B}_{\mathrm{mf}}+\boldsymbol{B}_{\mathrm{f}}\right)\delta\boldsymbol{U}_{\mathrm{e}} \tag{43}$$

In which the expression of $\mathbf{B}_{mf}$ and $\mathbf{B}_{f}$ are given by

$$\mathbf{B}_{\mathrm{mf}}=\left[\mathbf{B}_{\mathrm{mf}}^{1}\quad\mathbf{B}_{\mathrm{mf}}^{2}\quad\mathbf{B}_{\mathrm{mf}}^{3}\quad\mathbf{B}_{\mathrm{mf}}^{4}\right],\ \mathbf{B}_{f}=\begin{bmatrix}\mathbf{0}\\ \mathbf{0}\\ N_{\mathrm{m},x}\mathbf{B}_{\mathrm{f0}}^{u}\\ N_{\mathrm{m},y}\mathbf{B}_{\mathrm{f0}}^{v}\\ N_{\mathrm{m},y}\mathbf{B}_{\mathrm{f0}}^{u}+N_{\mathrm{m},x}\mathbf{B}_{\mathrm{f0}}^{v}\end{bmatrix} \tag{44}$$

where

$$\boldsymbol{B}_{\mathrm{mf}}^{i}=\begin{bmatrix}N_{i,x}&0&0&0&0&0&0\\ 0&N_{i,y}&0&0&0&0&0\\ N_{i,y}&N_{i,x}&0&0&0&0&0\\ 0&0&0&N_{i,x}&0&0&0\\ 0&0&0&0&N_{i,y}&0&0\\ 0&0&0&N_{i,y}&N_{i,x}&0&0\\ 0&0&0&0&0&N_{i,x}&0\\ 0&0&0&0&0&0&N_{i,y}\\ 0&0&0&0&0&N_{i,y}&N_{i,x}\end{bmatrix},\quad i=\overline{1,4} \tag{45}$$

The variation of the shear strain vector can be expressed in the matrix form as

$$\delta\boldsymbol{\gamma}_1=\boldsymbol{B}_{\mathrm{s}}\delta\boldsymbol{U}_{\mathrm{e}} \tag{46}$$

where

$$\begin{aligned}\boldsymbol{B}_{\mathrm{s}}&=\left[\boldsymbol{B}_{\mathrm{s}}^{1}\quad\boldsymbol{B}_{\mathrm{s}}^{2}\quad\boldsymbol{B}_{\mathrm{s}}^{3}\quad\boldsymbol{B}_{\mathrm{s}}^{4}\right],\\ \boldsymbol{B}_{\mathrm{s}}^{i}&=\begin{bmatrix}0&0&N_{i,x}&N_i&0&0&0\\ 0&0&N_{i,y}&0&N_i&0&0\end{bmatrix},\ i=\overline{1,4}\end{aligned} \tag{47}$$

By inserting Eqs. (43) and (46) into the expression of the variation of the strain energy, one gets

$$\delta\Pi=\int_A\delta\boldsymbol{U}_{\mathrm{e}}^{\mathrm{T}}\left(\boldsymbol{B}_{\mathrm{mf}}+\boldsymbol{B}_{\mathrm{f}}\right)^{\mathrm{T}}\boldsymbol{H}\left(\boldsymbol{B}_{\mathrm{mf}}+\boldsymbol{B}_{\mathrm{f}}\right)\boldsymbol{U}_{\mathrm{e}}\mathrm{d}A+\int_A\delta\boldsymbol{U}_{\mathrm{e}}^{\mathrm{T}}\boldsymbol{B}_{\mathrm{s}}^{\mathrm{T}}\boldsymbol{H}_{\mathrm{s}}\boldsymbol{B}_{\mathrm{s}}\boldsymbol{U}_{\mathrm{e}}\mathrm{d}A \tag{48}$$

The variation of work done by external force in terms of nodal displacements are obtained as the following formula

$$\delta W=\int_A\delta\boldsymbol{U}_{\mathrm{e}}^{\mathrm{T}}\boldsymbol{N}_{\mathrm{w}}^{\mathrm{T}}q\mathrm{d}A \tag{49}$$

where $\boldsymbol{N}_{\mathrm{w}}$ is given by

$$\begin{aligned}\boldsymbol{N}_{\mathrm{w}}&=\left[\boldsymbol{N}_{\mathrm{w1}}\quad\boldsymbol{N}_{\mathrm{w2}}\quad\boldsymbol{N}_{\mathrm{w3}}\quad\boldsymbol{N}_{\mathrm{w4}}\right],\\ \boldsymbol{N}_{\mathrm{w}i}&=\left[0\quad 0\quad N_i\quad 0\quad 0\quad 0\quad 0\right],\ i=\overline{1,4}\end{aligned} \tag{50}$$

The variation of work done by compressive load are calculated as following formula

$$\delta V_{\mathrm{E}}=\delta\boldsymbol{U}_{\mathrm{e}}^{\mathrm{T}}\int_S(\Delta\boldsymbol{N})^{\mathrm{T}}\boldsymbol{S}^{0}(\Delta\boldsymbol{N})\mathrm{d}S\boldsymbol{U}_{\mathrm{e}}=\delta\boldsymbol{U}_{\mathrm{e}}^{\mathrm{T}}\int_S\left(\boldsymbol{\Gamma}^{\mathrm{T}}\boldsymbol{S}^{0}\boldsymbol{\Gamma}\right)\mathrm{d}S\boldsymbol{U}_{\mathrm{e}} \tag{51}$$

where $\boldsymbol{\Gamma}$ is given by

$$\boldsymbol{\Gamma}=\Delta\boldsymbol{N},\quad \Delta=\mathrm{diag}(\nabla,\nabla,\nabla,\nabla,\nabla,\nabla,\nabla) \tag{52}$$

The variation of kinetic energy is obtained as the following formula

$$\delta T=\frac{1}{2}\int_A\int_z\left(\boldsymbol{N}\delta\dot{\boldsymbol{U}}_{\mathrm{e}}\right)^{\mathrm{T}}\boldsymbol{L}^{\mathrm{T}}\rho\boldsymbol{L}\left(\boldsymbol{N}\dot{\boldsymbol{U}}_{\mathrm{e}}\right)\mathrm{d}z\mathrm{d}A=\frac{1}{2}\int_A\delta\dot{\boldsymbol{U}}_{\mathrm{e}}^{\mathrm{T}}\boldsymbol{N}^{\mathrm{T}}\boldsymbol{I}_0\boldsymbol{N}\dot{\boldsymbol{U}}_{\mathrm{e}}\mathrm{d}A \tag{53}$$

Inserting Eqs. 48–52 into (15), and using the trivial manner of classical FEM, one gets the finite element equations of static bending, free vibration and buckling problem of the plates.

For the bending problem

$$\boldsymbol{K}\boldsymbol{U}=\boldsymbol{f} \tag{54}$$

For the free vibration problem

$$\left(\boldsymbol{K}-\omega^2\boldsymbol{M}\right)\boldsymbol{U}=0 \tag{55}$$

For the buckling problem

$$(\boldsymbol{K}-\lambda\boldsymbol{K}_{\mathrm{g}})\boldsymbol{U}=0 \tag{56}$$

In which, $\boldsymbol{K}$, $\boldsymbol{M}$, $\boldsymbol{K}_{\mathrm{g}}$, $\boldsymbol{f}$, $\boldsymbol{U}$ are respectively the global stiffness matrix, the global mass matrix, the global geometric stiffness matrix, the global nodal force vector and global displacement vector of the plate. These matrices and vectors are assembled by the element stiffness matrix $\boldsymbol{K}_{\mathrm{e}}$, the element mass matrix $\boldsymbol{M}_{\mathrm{e}}$, the element geometric stiffness matrix $\boldsymbol{K}_{\mathrm{ge}}$ and the element nodal force vector $\boldsymbol{f}_{\mathrm{e}}$. They are computed by the following formulae

$$\boldsymbol{K}_{\mathrm{e}}=\boldsymbol{L}_{\mathrm{mf}}+\boldsymbol{L}_{\mathrm{s}} \tag{57}$$

$$\boldsymbol{L}_{\mathrm{mf}}=\int_A\left(\boldsymbol{B}_{\mathrm{mf}}+\boldsymbol{B}_{\mathrm{f}}\right)^{\mathrm{T}}\boldsymbol{H}\left(\boldsymbol{B}_{\mathrm{mf}}+\boldsymbol{B}_{\mathrm{f}}\right)\mathrm{d}A \tag{58}$$

$$\boldsymbol{L}_{\mathrm{s}}=\int_A\boldsymbol{B}_{\mathrm{s}}^{\mathrm{T}}\boldsymbol{H}_{\mathrm{s}}\boldsymbol{B}_{\mathrm{s}}\mathrm{d}A \tag{59}$$

$$\boldsymbol{K}_{\mathrm{ge}}=\int_A\boldsymbol{\Gamma}^{\mathrm{T}}\boldsymbol{S}^0\boldsymbol{\Gamma}\mathrm{d}A \tag{60}$$

$$\boldsymbol{M}_{\mathrm{e}}=\int_A\boldsymbol{N}^{\mathrm{T}}\boldsymbol{I}_0\boldsymbol{N}\mathrm{d}A \tag{61}$$

Table 1
The convergency and comparison of the non-dimensional center deflection of FG sandwich plates.

p	Method	1-0-1	1-2-1	1-1-1	2-2-1	1-2-1
0	Present (2 × 2)	0.15980	0.15980	0.15980	0.15980	0.15980
	Present (8 × 8)	0.19342	0.19342	0.19342	0.19342	0.19342
	Present (16 × 16)	0.19540	0.19540	0.19540	0.19540	0.19540
	Present (32 × 32)	0.19590	0.19590	0.19590	0.19590	0.19590
	Present (40 × 40)	0.19596	0.19596	0.19596	0.19596	0.19596
	Zenkour [12] (TSDT)	0.19606	0.19606	0.19606	0.19606	0.19606
	Zenkour [12] (SSDT)	0.19605	0.19605	0.19605	0.19605	0.19605
1	Present (2 × 2)	0.26399	0.22333	0.23963	0.23963	0.22333
	Present (8 × 8)	0.31925	0.26739	0.28813	0.28813	0.26739
	Present (16 × 16)	0.32251	0.27005	0.29103	0.29103	0.27005
	Present (32 × 32)	0.32333	0.27072	0.29176	0.29176	0.27072
	Present (40 × 40)	0.32343	0.27080	0.29185	0.29185	0.27080
	Zenkour [12] (TSDT)	0.32358	0.30632	0.29199	0.28085	0.27094
	Zenkour [12] (SSDT)	0.32349	0.30624	0.29194	0.28082	0.27093
2	Present (2 × 2)	0.30269	0.24969	0.27220	0.27220	0.24969
	Present (8 × 8)	0.36828	0.29868	0.32845	0.32845	0.29868
	Present (16 × 16)	0.37210	0.30164	0.33179	0.33179	0.30164
	Present (32 × 32)	0.37307	0.30238	0.33263	0.33263	0.30238
	Present (40 × 40)	0.37319	0.30247	0.33273	0.33273	0.30247
	Zenkour [12] (TSDT)	0.37335	0.35231	0.33289	0.31617	0.30263
	Zenkour [12] (SSDT)	0.37319	0.35218	0.3328	0.31611	0.30260
5	Present (2 × 2)	0.33061	0.27475	0.30103	0.30103	0.27475
	Present (8 × 8)	0.40368	0.33037	0.36640	0.36640	0.33037
	Present (16 × 16)	0.40791	0.33370	0.37021	0.37021	0.33370
	Present (32 × 32)	0.40898	0.33454	0.37118	0.37118	0.33454
	Present (40 × 40)	0.40911	0.33464	0.37129	0.37129	0.33464
	Zenkour [12] (TSDT)	0.40927	0.39183	0.37145	0.34960	0.33480
	Zenkour [12] (SSDT)	0.40905	0.3916	0.37128	0.34950	0.33474

Table 2
The comparison of the non-dimensional axial stress of FG sandwich plates.

p	Method	1-0-1	1-2-1	1-1-1	2-2-1	1-2-1
0	Present	1.99178	1.99178	1.99178	1.99178	1.99178
	Zenkour [12] (TSDT)	2.04985	2.04985	2.04985	2.04985	2.04985
	Zenkour [12] (SSDT)	2.05452	2.05452	2.05452	2.05452	2.05452
1	Present	1.54246	1.29012	1.39234	1.39234	1.29012
	Zenkour [12] (TSDT)	1.57923	1.49587	1.42617	1.32062	1.32309
	Zenkour [12] (SSDT)	1.58204	1.49859	1.42892	1.32342	1.32590
2	Present	1.78157	1.44532	1.59201	1.59201	1.44532
	Zenkour [12] (TSDT)	1.82167	1.72144	1.62748	1.47095	1.47988
	Zenkour [12] (SSDT)	1.82450	1.72412	1.63025	1.47387	1.48283
5	Present	1.94773	1.60268	1.77944	1.77944	1.60268
	Zenkour [12] (TSDT)	1.99272	1.91302	1.8158	1.61181	1.63814
	Zenkour [12] (SSDT)	1.99567	1.91547	1.81838	1.61477	1.64106

Table 3
The comparison of the non-dimensional shear stress of FG sandwich plates.

p	Method	1-0-1	1-2-1	1-1-1	2-2-1	1-2-1
0	Present	0.22930	0.22930	0.22930	0.22930	0.22930
	Zenkour [12] (TSDT)	0.23857	0.23857	0.23857	0.23857	0.23857
	Zenkour [12] (SSDT)	0.24618	0.24618	0.24618	0.24618	0.24618
1	Present	0.27853	0.24078	0.24881	0.24881	0.24078
	Zenkour [12] (TSDT)	0.29203	0.27104	0.26117	0.25951	0.25258
	Zenkour [12] (SSDT)	0.29907	0.27774	0.26809	0.2668	0.26004
2	Present	0.31115	0.24557	0.25836	0.25836	0.24557
	Zenkour [12] (TSDT)	0.32622	0.28838	0.27188	0.26939	0.25834
	Zenkour [12] (SSDT)	0.33285	0.29422	0.27807	0.27627	0.26543
5	Present	0.36976	0.25148	0.27195	0.27195	0.25148
	Zenkour [12] (TSDT)	0.38634	0.31454	0.28643	0.28265	0.26512
	Zenkour [12] (SSDT)	0.39370	0.31930	0.29150	0.28895	0.27153

Table 4
The convergency and comparison of the non-dimensional center deflection of FGSP with porosity.

ξ	Method	1-0-1	1-1-1	1-2-1	2-1-2	2-2-1
0	Present (2 × 2)	0.30269	0.27220	0.24969	0.28655	0.25933
	Present (8 × 8)	0.36828	0.32845	0.29868	0.34756	0.31198
	Present (16 × 16)	0.37210	0.33179	0.30164	0.35115	0.31512
	Present (32 × 32)	0.37307	0.33263	0.30238	0.35205	0.31592
	Present (40 × 40)	0.37319	0.33273	0.30247	0.35216	0.31601
	Daikh and Zenkour [25]	0.37326	0.33283	0.30262	0.35224	0.31614
0.1	Present (2 × 2)	0.35702	0.31414	0.28173	0.33458	0.29541
	Present (8 × 8)	0.43557	0.37902	0.33573	0.40657	0.35491
	Present (16 × 16)	0.44014	0.38288	0.33903	0.41079	0.35848
	Present (32 × 32)	0.44130	0.38385	0.33986	0.41186	0.35938
	Present (40 × 40)	0.44144	0.38397	0.33996	0.41199	0.35949
	Daikh and Zenkour [25]	0.44152	0.38408	0.34012	0.41208	0.35963
0.2	Present (2 × 2)	0.43217	0.36958	0.32210	0.39968	0.34209
	Present (8 × 8)	0.52830	0.44487	0.38116	0.48588	0.40960
	Present (16 × 16)	0.53389	0.44938	0.38484	0.49094	0.41369
	Present (32 × 32)	0.53530	0.45052	0.38577	0.49222	0.41472
	Present (40 × 40)	0.53547	0.45066	0.38589	0.49237	0.41485
	Daikh and Zenkour [25]	0.53558	0.45079	0.38606	0.49248	0.41501

Table 5
The comparison of the non-dimensional axial stress of FGSP with porosity.

ξ	Method	1-0-1	1-1-1	1-2-1	2-1-2	2-2-1
0	Present	1.78061	1.59120	1.44463	1.68389	1.43449
	Daikh and Zenkour [25]	1.78397	1.59409	1.44725	1.68697	1.43712
0.1	Present	1.70550	1.48770	1.31517	1.59596	1.30495
	Daikh and Zenkour [25]	1.70865	1.49029	1.31746	1.59879	1.30725
0.2	Present	1.61925	1.36725	1.16859	1.49357	1.16225
	Daikh and Zenkour [25]	1.62215	1.36952	1.17052	1.49611	1.16421

Table 6
The comparison of the non-dimensional shear stress of FGSP with porosity.

ξ	Method	1-0-1	1-1-1	1-2-1	2-1-2	2-2-1
0	Present	0.30400	0.25197	0.23977	0.26754	0.25016
	Daikh and Zenkour [25]	0.32991	0.27529	0.26224	0.29161	0.27318
0.1	Present	0.31157	0.25804	0.24278	0.27834	0.25581
	Daikh and Zenkour [25]	0.35817	0.28392	0.26722	0.30541	0.28114
0.2	Present	0.32099	0.26459	0.24603	0.29046	0.26191
	Daikh and Zenkour [25]	0.39364	0.29385	0.27292	0.32158	0.29020

$$\boldsymbol{f}_{\mathrm{e}} = \int_{A} \boldsymbol{N}_{\mathrm{w}}^{\mathrm{T}} q \mathrm{d}A \tag{62}$$

3. Numerical results and discussions

3.1. Convergency and verification study

To verify the convergent rate and the accuracy of the present algorithm, some comparisons between the results of the present procedure with published data will be considered in this subsection.

Firstly, a square FGM sandwich plates with one homogenous ceramic core of ZrO_2 and two FGM face sheets of Al/ZrO_2 is examined. Young's modulus of ZrO_2 and Al are $E_c = 151$ GPaand $E_m = 70$ GPa, respectively; while the Poisson's ratio is constant $\nu = 0.3$, and the side-to-thickness ratio of the plate is $a/h = 10$. The plate is simply supported at all edges and subjected to sinusoidal load. The non-dimensional center deflections, axial and shear stresses are computed as the following formulae ($E_0 = 1$ GPa)

$$\overline{w} = \frac{10hE_0}{a^2 q_0} w\left(\frac{a}{2}, \frac{b}{2}\right), \ \overline{\sigma}_x = \frac{10h^2}{a^2 q_0}\sigma_x\left(\frac{a}{2}, \frac{b}{2}, \frac{h}{2}\right), \ \overline{\tau}_{xz} = \frac{h}{aq_0}\tau_x\left(0, \frac{b}{2}, 0\right) \tag{63}$$

Table 1 presents the comparison between the present numerical results and those of Zenkour [12] of an FG sandwich plate without porosity. It can see clearly that the numerical results converge at the mesh of 32×32. The results in Tables 2 and 3 are calculated using the mesh of 32×32. According to Tables 1–3, the present results at the mesh of 32×32 are in good agreement with the results of Zenkour [12] using TSDT and SSDT.

Next, the authors examine the static bending of a square FGSP of Al/ZrO_2 with different values of porosity coefficients. The geometry and materials properties are similar to those of previous comparison, the volume fraction index is $p = 2$. It is noticed that this sandwich plate is achieved easily from FGSP of porosity I by setting two metal ingredients at the bottom and top layer with similar material properties. The present results are compared with those of Daikh and Zenkour [25] using an analytical solution. The comparison the non-dimensional center deflections, axial stress and transverse shear stress are presented in Tables 4–6. It is obvious that the numerical results converge at the mesh of 32×32, and close to the results of Daikh and Zenkour [25] using the analytical solution.

Secondly, the non-dimensional frequency and critical buckling load of a square FG sandwich of Al/Al_2O_3 using the present algorithm are compared to those of Zenkour [13] using TSDT and SSDT. In this examination, the square FG sandwich plate is made of one homogenous ceramic core of Al_2O_3, two similar FGM face sheets of Al/Al_2O_3, and the side-to-thickness ratio of $a/h = 10$. The material properties of Al_2O_3 are $E_c = 380$ GPa, $\rho_c = 3800$ kg/m^3, $\nu = 0.3$, and those of Al are $E_m = 70$ GPa, $\rho_m = 2707$ kg/m^3,$\nu = 0.3$. The following non-dimensional parameters are used

$$\overline{\omega} = \omega \frac{a^2}{h}\sqrt{\frac{\rho_0}{E_0}}, \ \overline{N}_{\mathrm{cr}} = N_{\mathrm{cr}}\frac{a^2}{100h^3E_0}, \ E_0 = 1 \text{ GPa}, \ \rho_0 = 1 \text{ kg/m}^3 \tag{64}$$

The numerical results of the present algorithm and those of Zenkour [13] are exhibited in Tables 7 and 8. It is obvious that the

Table 7
The convergency and comparison of the non-dimensional frequency of FG sandwich plates.

p	Method	1-0-1	2-1-2	2-1-1	1-1-1	2-2-1	1-2-1
0	Present (2×2)	2.38279	2.38279	2.38279	2.38279	2.38279	2.38279
	Present (8×8)	1.85410	1.85410	1.85410	1.85410	1.85410	1.85410
	Present (16×16)	1.83181	1.83181	1.83181	1.83181	1.83181	1.83181
	Present (32×32)	1.82629	1.82629	1.82629	1.82629	1.82629	1.82629
	Present (40×40)	1.82563	1.82563	1.82563	1.82563	1.82563	1.82563
	Zenkour [13] (TSDT)	1.82445	1.82445	1.82445	1.82445	1.82445	1.82445
	Zenkour [13] (SSDT)	1.82452	1.82452	1.82452	1.82452	1.82452	1.82452
0.5	Present (2×2)	1.87122	1.92111	1.95019	1.96498	2.00212	2.03518
	Present (8×8)	1.46728	1.50772	1.53041	1.54338	1.57179	1.59954
	Present (16×16)	1.44994	1.48994	1.51236	1.52521	1.55327	1.58074
	Present (32×32)	1.44564	1.48553	1.50789	1.52071	1.54868	1.57609
	Present (40×40)	1.44513	1.48500	1.50735	1.52017	1.54813	1.57553
	Zenkour [13] (TSDT)	1.44424	1.48408	1.51253	1.51922	1.55199	1.57451
	Zenkour [13] (SSDT)	1.44436	1.48418	1.51258	1.51927	1.55202	1.57450
1	Present (2×2)	1.60331	1.67077	1.71394	1.73411	1.78997	1.83933
	Present (8×8)	1.26283	1.32049	1.35432	1.37442	1.41746	1.46166
	Present (16×16)	1.24804	1.30515	1.33858	1.35856	1.40107	1.44490
	Present (32×32)	1.24437	1.30135	1.33468	1.35462	1.39701	1.44074
	Present (40×40)	1.24393	1.30089	1.33421	1.35415	1.39652	1.44024
	Zenkour [13] (TSDT)	1.24320	1.30011	1.34888	1.35333	1.40789	1.43934
	Zenkour [13] (SSDT)	1.24335	1.30023	1.34894	1.35339	1.40792	1.43931
5	Present (2×2)	1.24506	1.28361	1.34153	1.34893	1.42682	1.48792
	Present (8×8)	0.96154	0.99779	1.04722	1.06121	1.12644	1.19186
	Present (16×16)	0.94976	0.98574	1.03468	1.04873	1.11328	1.17842
	Present (32×32)	0.94685	0.98276	1.03157	1.04564	1.11002	1.17508
	Present (40×40)	0.94650	0.98240	1.03120	1.04527	1.10963	1.17468
	Zenkour [13] (TSDT)	0.94598	0.98184	1.07432	1.04466	1.14731	1.17397
	Zenkour [13] (SSDT)	0.94630	0.98207	1.07445	1.04481	1.14741	1.17399

Table 8
The comparison of the non-dimensional critical buckling load of FG sandwich plates.

p	Method	1-0-1	1-1-1	1-2-1	2-1-2	2-2-1	2-1-1
0	Present (2 × 2)	11.98620	11.98620	11.98620	11.98620	11.98620	11.98620
	Present (8 × 8)	6.61972	6.61972	6.61972	6.61972	6.61972	6.61972
	Present (16 × 16)	6.45984	6.45984	6.45984	6.45984	6.45984	6.45984
	Present (32 × 32)	6.42089	6.42089	6.42089	6.42089	6.42089	6.42089
	Present (40 × 40)	6.41624	6.41624	6.41624	6.41624	6.41624	6.41624
	Zenkour [13] (TSDT)	6.50248	6.50248	6.50248	6.50248	6.50248	6.50248
	Zenkour [13] (SSDT)	6.50303	6.50303	6.50303	6.50303	6.50303	6.50303
0.5	Present (2 × 2)	6.67085	7.17967	7.43750	7.61543	7.96074	8.30996
	Present (8 × 8)	3.74432	4.03723	4.18139	4.28915	4.47910	4.68612
	Present (16 × 16)	3.65548	3.94165	4.08238	4.18781	4.37316	4.57558
	Present (32 × 32)	3.63382	3.91834	4.05824	4.16309	4.34733	4.54862
	Present (40 × 40)	3.63124	3.91556	4.05536	4.16014	4.34424	4.54540
	Zenkour [13] (TSDT)	3.68219	3.97042	4.11235	4.21823	4.40499	4.60841
	Zenkour [13] (SSDT)	3.68284	3.97097	4.11269	4.21856	4.40519	4.60835
1	Present (2 × 2)	4.63547	5.20108	5.51782	5.72375	6.16348	6.61062
	Present (8 × 8)	2.62572	2.96698	3.14629	3.28388	3.52989	3.81288
	Present (16 × 16)	2.56401	2.89780	3.07290	3.20782	3.44799	3.72513
	Present (32 × 32)	2.54895	2.88092	3.05499	3.18926	3.42800	3.70371
	Present (40 × 40)	2.54716	2.87891	3.05285	3.18704	3.42561	3.70115
	Zenkour [13] (TSDT)	2.58357	2.92003	3.09697	3.23237	3.47472	3.75328
	Zenkour [13] (SSDT)	2.58423	2.92060	3.09731	3.23270	3.47490	3.75314
5	Present (2 × 2)	2.48482	2.80422	3.10767	3.21744	3.66736	4.09886
	Present (8 × 8)	1.35242	1.54703	1.72908	1.81860	2.08772	2.40286
	Present (16 × 16)	1.31917	1.50954	1.68754	1.77571	2.03882	2.34845
	Present (32 × 32)	1.31107	1.50041	1.67741	1.76524	2.02689	2.33516
	Present (40 × 40)	1.31011	1.49932	1.67620	1.76399	2.02547	2.33357
	Zenkour [13] (TSDT)	1.32910	1.52129	1.70176	1.78978	2.05605	2.36734
	Zenkour [13] (SSDT)	1.33003	1.52203	1.70224	1.79032	2.05644	2.36744

Table 9
The convergency and comparison of the non-dimensional frequency of FGSP with porosity.

ξ	Method	1-0-1	1-1-1	1-2-1	2-1-2	2-2-1	2-1-1
0	Present (2 × 2)	1.37808	1.51826	1.64927	1.44506	1.58889	1.49887
	Present (8 × 8)	1.07843	1.20683	1.32227	1.14006	1.26316	1.18358
	Present (16 × 16)	1.06561	1.19298	1.30739	1.12674	1.24867	1.16978
	Present (32 × 32)	1.06243	1.18954	1.30370	1.12345	1.24507	1.16636
	Present (40 × 40)	1.06205	1.18913	1.30326	1.12305	1.24464	1.16595
	Daikh and Zenkour [26]	1.06155	1.18847	1.30244	1.12248	1.24391	1.16529
0.1	Present (2 × 2)	1.26860	1.41866	1.56616	1.33770	1.49820	1.39811
	Present (8 × 8)	0.99806	1.13772	1.26797	1.06328	1.19998	1.11053
	Present (16 × 16)	0.98632	1.12490	1.25400	1.05106	1.18642	1.09773
	Present (32 × 32)	0.98341	1.12172	1.25053	1.04803	1.18305	1.09455
	Present (40 × 40)	0.98307	1.12134	1.25012	1.04766	1.18265	1.09417
	Daikh and Zenkour [26]	0.98258	1.12071	1.24933	1.04712	1.18195	1.09355
0.2	Present (2 × 2)	1.11837	1.29766	1.47126	1.20049	1.39023	1.27136
	Present (8 × 8)	0.89214	1.05732	1.20880	0.96920	1.12709	1.02089
	Present (16 × 16)	0.88195	1.04581	1.19590	0.95842	1.11466	1.00937
	Present (32 × 32)	0.87943	1.04295	1.19269	0.95574	1.11157	1.00651
	Present (40 × 40)	0.87912	1.04260	1.19231	0.95542	1.11120	1.00616
	Daikh and Zenkour [26]	0.87867	1.04201	1.19156	0.95491	1.11054	1.00557

frequency and critical buckling load of the sandwich plate converge at the mesh of 32 × 32 and those are very closed to the results of Zenkour [13].

Continuously, the non-dimensional frequency and critical buckling load of FG sandwich plates of Al/Al_2O_3 with porosity using the present algorithm are compared to those of Daikh and Zenkour [26] using an analytical method. In this examination, the square FGSP is made of one homogenous ceramic core of Al_2O_3, two similar FGM face sheets of Al/Al_2O_3. The geometry and materials properties are similar to those of previous comparison, the volume fraction index is $p = 2$. The numerical results of the present algorithm and those of Daikh and Zenkour [26] are performed in Tables 9 and 10. It is obvious that the frequency and critical buckling load of the sandwich plate converge at the mesh of 32× 32 and those are very closed to the results of Daikh and Zenkour [26].

According to several comparison studies, the numerical results of the present algorithm converge at the mesh of 32 × 32, and are in good agreement with published results. Hence, in the rest of the paper, the mesh of 32 × 32 is used to investigate the mechanical behavior of the FGSP with porosity.

3.2. Parameter study and discussions

In the recent work, the FGSP contains one homogenous ceramic core of Al_2O_3, one bottom face sheet of Al/Al_2O_3 and one top face sheet of $SUS304/Al_2O_3$. The material properties of Al_2O_3 are $E_c = 380$ GPa, $\rho_c = 3800$ kg/m^3, $\nu = 0.3$, those of Al are $E_b = 70$ GPa, $\rho_b = 2707$ kg/m^3, $\nu = 0.3$, and those of SUS304 are $E_t = 207$ GPa, $\rho_t = 8166$ kg/m^3, $\nu = 0.3$. The effective Young's modulus and mass density through the thickness of the (1-1-1) perfect FGSP are

Table 10
The comparison of the non-dimensional critical buckling load of FGSP with porosity.

ξ	Method	1-0-1	1-1-1	1-2-1	2-1-2	2-2-1	2-1-1
0	Present (2 × 2)	3.23337	4.23062	5.17442	3.72137	4.70103	4.04855
	Present (8 × 8)	1.80770	2.44165	3.03866	2.11528	2.71401	2.30550
	Present (16 × 16)	1.76457	2.38541	2.97006	2.06572	2.65152	2.25156
	Present (32 × 32)	1.75405	2.37168	2.95329	2.05362	2.63626	2.23840
	Present (40 × 40)	1.75280	2.37004	2.95129	2.05218	2.63444	2.23683
	Daikh and Zenkour [26]	1.77856	2.40449	2.99342	2.08228	2.67334	2.27031
0.1	Present (2 × 2)	2.44896	3.44813	4.43923	2.92840	3.93224	3.25514
	Present (8 × 8)	1.38406	2.02670	2.66009	1.69026	2.30549	1.87636
	Present (16 × 16)	1.35139	1.98090	2.60131	1.65128	2.25322	1.83296
	Present (32 × 32)	1.34342	1.96971	2.58693	1.64176	2.24045	1.82237
	Present (40 × 40)	1.34247	1.96837	2.58521	1.64062	2.23892	1.82110
	Daikh and Zenkour [26]	1.36232	1.99718	2.62234	1.66484	2.27248	1.84884
0.2	Present (2 × 2)	1.67704	2.67936	3.71711	2.14854	3.17253	2.47038
	Present (8 × 8)	0.97464	1.62659	2.29569	1.27996	1.90694	1.45601
	Present (16 × 16)	0.95230	1.59108	2.24657	1.25141	1.86479	1.42306
	Present (32 × 32)	0.94685	1.58238	2.23454	1.24443	1.85448	1.41500
	Present (40 × 40)	0.94620	1.58135	2.23311	1.24360	1.85325	1.41404
	Daikh and Zenkour [26]	0.96028	1.60465	2.26539	1.26208	1.88149	1.43604

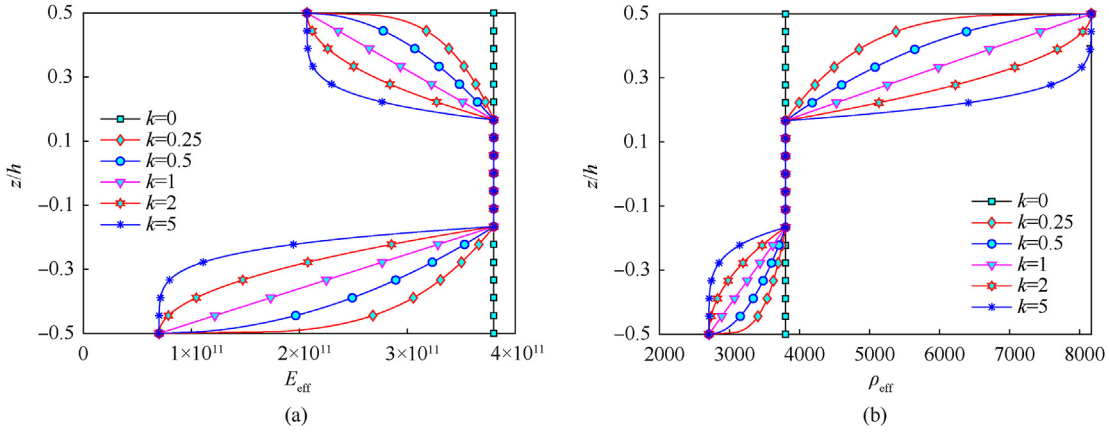

Fig. 2. The effective Young's modulus and mass density of perfect FGSP.

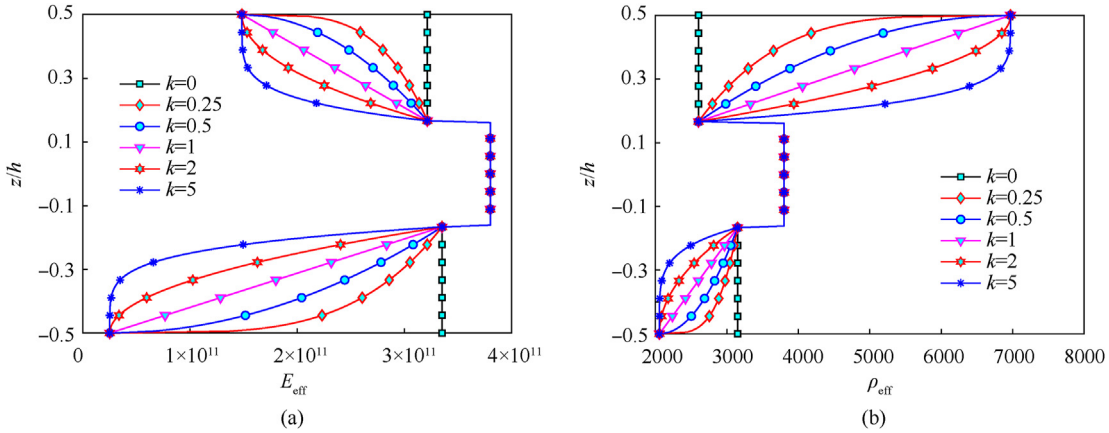

Fig. 3. The effective Young's modulus and mass density of FGSP with porosity I ($\xi = 0.2$).

demonstrated in Fig. 2. Figs. 3–5 presents the effective Young's modulus and mass density through the thickness of the (1-1-1) FGSP with porosity. In two cases of porosity I and porosity II, the porosity reduces the effective Young's modulus and mass density of the materials at two face sheets, while the porosity III reduces the effective Young's modulus and mass density of the material at the ceramic core of the sandwich plates.

Four types of boundary conditions of the plate are considered, which are fully clamped at all edges (CCCC), fully simply supported at all edges (SSSS), clamped at two opposite edges and simply supported at two opposite edges (SCSC), and clamped at two continuous edges and simply supported at next two edges (SSCC).

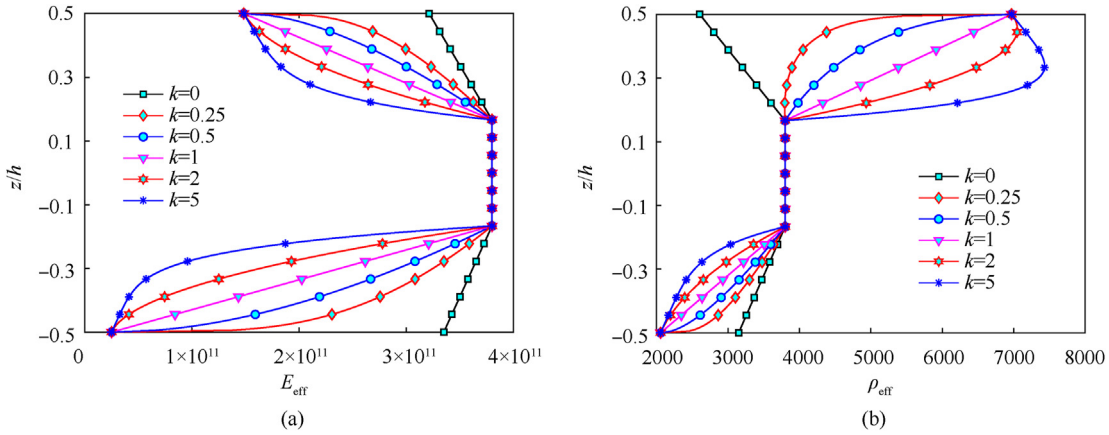

Fig. 4. The effective Young's modulus and mass density of FGSP with porosity II ($\xi = 0.2$).

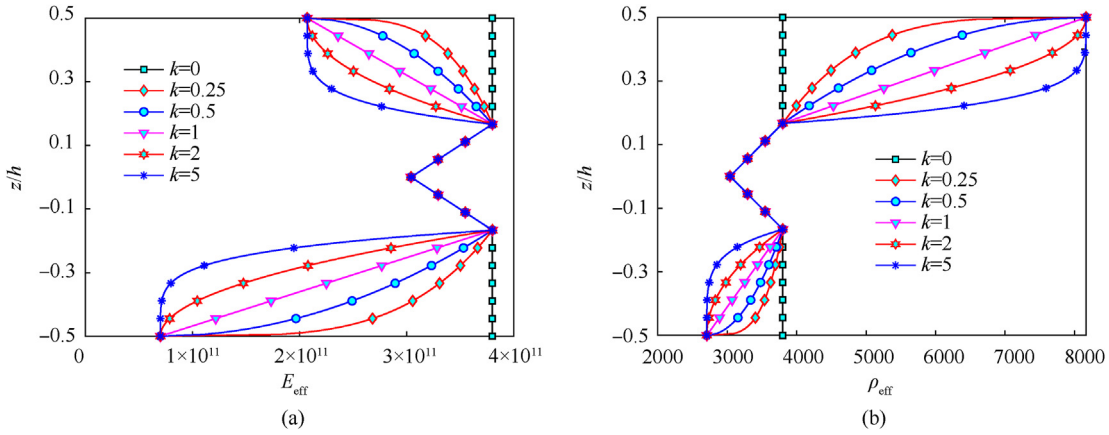

Fig. 5. The effective Young's modulus and mass density of FGSP with porosity III ($\xi = 0.2$).

Table 11
The non-dimensional center deflections of FGSP with porosity.

Porosity	ξ	p	1-0-1	1-1-1	1-2-1	2-1-2	2-2-1	2-1-1
Perfect	0	0	0.07784	0.07784	0.07784	0.07784	0.07784	0.07784
		2	0.19109	0.15673	0.13592	0.17193	0.15864	0.17887
		10	0.24594	0.20065	0.16784	0.22211	0.20828	0.23712
Porosity I	0.1	0	0.08493	0.08454	0.08386	0.08480	0.08389	0.08432
		2	0.23407	0.18315	0.15343	0.20534	0.18511	0.21586
		10	0.32501	0.24499	0.19456	0.28046	0.25764	0.31023
	0.2	0	0.09299	0.09209	0.09051	0.09268	0.09059	0.09157
		2	0.29909	0.21860	0.17511	0.25259	0.22089	0.27043
		10	0.47842	0.31147	0.22984	0.37627	0.33571	0.44758
Porosity II	0.1	0	0.08300	0.08211	0.08141	0.08253	0.08162	0.08211
		2	0.22091	0.17288	0.14592	0.19354	0.17445	0.20243
		10	0.29786	0.22751	0.18310	0.25915	0.23732	0.28251
	0.2	0	0.08863	0.08668	0.08517	0.08761	0.08561	0.08668
		2	0.26039	0.19211	0.15715	0.22046	0.19327	0.23244
		10	0.37557	0.26159	0.20087	0.30940	0.27497	0.34851
Porosity III	0.1	0	0.07784	0.07802	0.07825	0.07792	0.07830	0.07814
		2	0.19109	0.15734	0.13704	0.17225	0.15948	0.17929
		10	0.24594	0.20186	0.16963	0.22294	0.20953	0.23763
	0.2	0	0.07784	0.07820	0.07867	0.07800	0.07876	0.07845
		2	0.19109	0.15796	0.13818	0.17258	0.16033	0.17973
		10	0.24594	0.20311	0.17146	0.22379	0.21078	0.23816

Table 12
The non-dimensional axial stress of FGSP with porosity.

Porosity	ξ	p	1-0-1	1-1-1	1-2-1	2-1-2	2-2-1	2-1-1
Perfect	0	0	1.99061	1.99061	1.99061	1.99061	1.99061	1.99061
		2	2.36072	2.04071	1.80772	2.19584	1.94116	2.12279
		10	2.75247	2.50872	2.17768	2.67675	2.39789	2.60347
Porosity I	0.1	0	1.93447	1.92622	1.90938	1.93224	1.89685	1.90985
		2	2.36329	1.97078	1.68829	2.16169	1.84558	2.07883
		10	2.90035	2.52517	2.08732	2.76812	2.40110	2.72709
	0.2	0	1.87754	1.85990	1.82542	1.87252	1.80104	1.82684
		2	2.39753	1.89420	1.55336	2.13503	1.74591	2.05296
		10	3.25626	2.57769	1.98653	2.95732	2.46079	3.04606
Porosity II	0.1	0	1.88788	1.86618	1.84896	1.87661	1.84447	1.85616
		2	2.24758	1.85908	1.60265	2.04051	1.74646	1.95971
		10	2.72074	2.34696	1.96135	2.57161	2.22755	2.51212
	0.2	0	1.78398	1.74169	1.70877	1.76190	1.70062	1.72280
		2	2.12517	1.66244	1.38876	1.86945	1.54184	1.78692
		10	2.72139	2.16908	1.73071	2.46239	2.04870	2.44052
Porosity III	0.1	0	1.99061	1.99317	1.99845	1.99133	2.00988	2.00455
		2	2.36072	2.04218	1.81652	2.19461	1.95474	2.13176
		10	2.75247	2.51090	2.19028	2.67475	2.41148	2.60959
	0.2	0	1.99061	1.99572	2.00625	1.99206	2.02948	2.01851
		2	2.36072	2.04353	1.82509	2.19337	1.96849	2.14081
		10	2.75247	2.51281	2.20250	2.67269	2.42502	2.61573

Table 13
The non-dimensional shear stress of FGSP with porosity.

Porosity	ξ	p	1-0-1	1-1-1	1-2-1	2-1-2	2-2-1	2-1-1
Perfect	0	0	0.22560	0.22560	0.22560	0.22560	0.22560	0.22560
		2	0.32286	0.25732	0.24289	0.27618	0.25987	0.28613
		10	0.46859	0.28207	0.25266	0.32705	0.28625	0.34939
Porosity I	0.1	0	0.22734	0.22964	0.22765	0.23192	0.22886	0.22238
		2	0.33496	0.26302	0.24581	0.28644	0.26441	0.28419
		10	0.50908	0.28828	0.25572	0.34129	0.29014	0.34743
	0.2	0	0.22942	0.23405	0.22985	0.23895	0.23238	0.21885
		2	0.34952	0.26906	0.24897	0.29764	0.26904	0.28119
		10	0.56002	0.29389	0.25891	0.35503	0.29201	0.33831
Porosity II	0.1	0	0.22880	0.22698	0.22648	0.22759	0.22679	0.22738
		2	0.33042	0.25956	0.24439	0.27957	0.26175	0.28913
		10	0.48497	0.28414	0.25421	0.33086	0.28743	0.35179
	0.2	0	0.23217	0.22841	0.22738	0.22965	0.22801	0.22922
		2	0.33829	0.26191	0.24599	0.28307	0.26368	0.29205
		10	0.50140	0.28612	0.25588	0.33421	0.28824	0.35247
Porosity III	0.1	0	0.22560	0.21290	0.21509	0.21094	0.22246	0.22915
		2	0.32286	0.24383	0.23220	0.25928	0.25758	0.29227
		10	0.46859	0.26826	0.24206	0.30828	0.28509	0.35907
	0.2	0	0.22560	0.19882	0.20313	0.19504	0.21913	0.23294
		2	0.32286	0.22872	0.21996	0.24077	0.25516	0.29887
		10	0.46859	0.25264	0.22986	0.28753	0.28389	0.36961

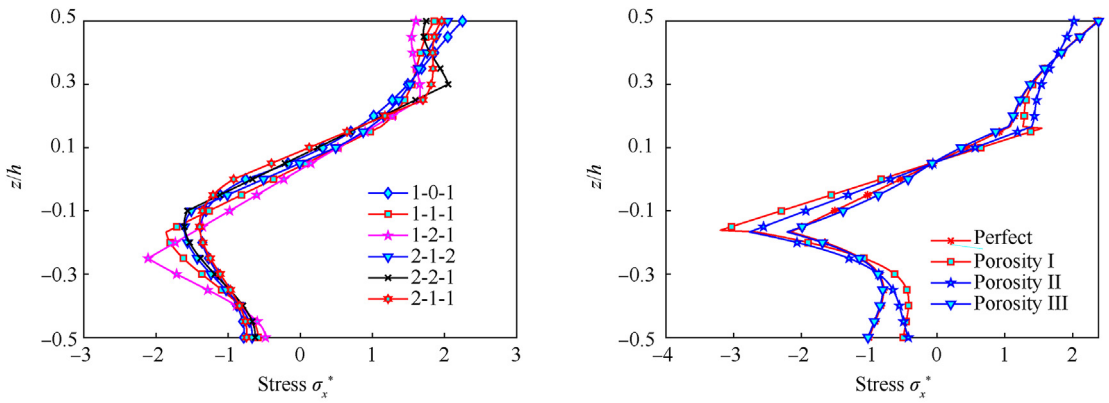

(a) Porosity II, b/a=1, a/h=10, p=2, ξ= 0.1 (b) (1-1-1), b/a=1, a/h=10, p=5, ξ= 0.2

Fig. 6. The distribution of the axial stress through the thickness of FGSP with porosity (SSSS).

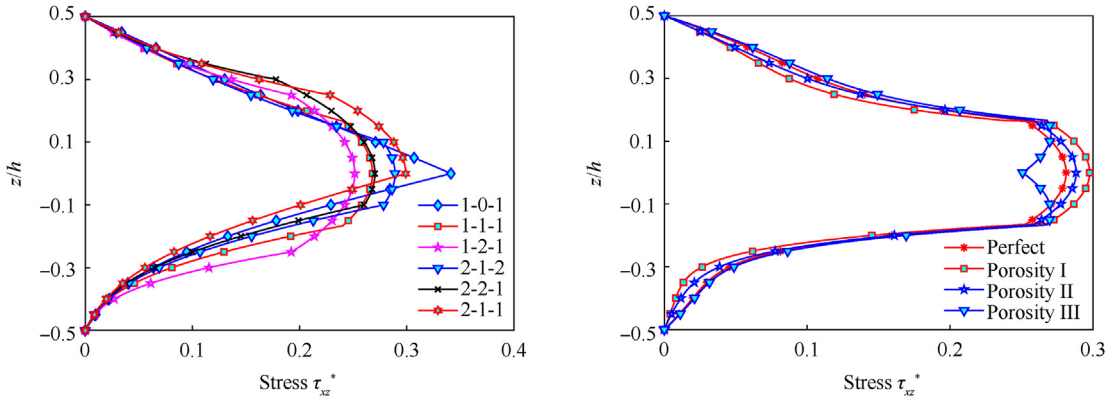

(a) Porosity II, b/a=1, a/h=10, p=2, ξ= 0.1 (b) (1-1-1), b/a=1, a/h=10, p=5, ξ= 0.2

Fig. 7. The distribution of the shear stress through the thickness of FGSP with porosity (SSSS).

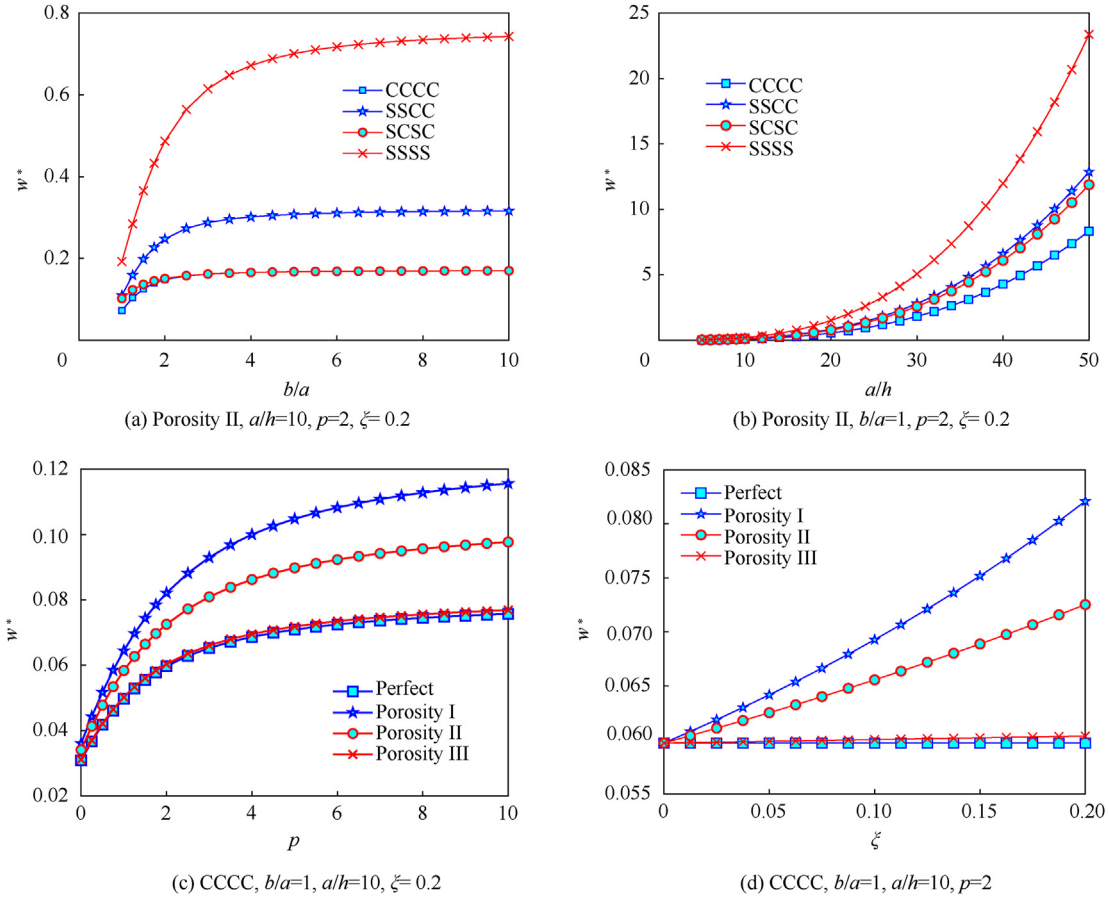

(a) Porosity II, a/h=10, p=2, ξ= 0.2 (b) Porosity II, b/a=1, p=2, ξ= 0.2

(c) CCCC, b/a=1, a/h=10, ξ= 0.2 (d) CCCC, b/a=1, a/h=10, p=2

Fig. 8. The effects of several parameters on the center deflection of the (1-1-1) FGSP with porosity.

Table 14
The non-dimensional fundamental frequency of FGSP with porosity (SSSS).

Porosity	ξ	p	1-0-1	1-1-1	1-2-1	2-1-2	2-2-1	2-1-1
Perfect	0	0	1.82629	1.82629	1.82629	1.82629	1.82629	1.82629
		2	1.02749	1.17836	1.29127	1.10772	1.23215	1.15030
		10	0.87183	1.01271	1.13653	0.94368	1.06179	0.98375
Porosity I	0.1	0	1.86540	1.82852	1.81619	1.84189	1.82052	1.83194
		2	0.97557	1.12927	1.24925	1.05628	1.17743	1.08889
		10	0.79390	0.94757	1.08370	0.87282	0.98465	0.89327
	0.2	0	1.92054	1.83532	1.80824	1.86551	1.81758	1.84283
		2	0.91187	1.07373	1.20391	0.99615	1.11504	1.01505
		10	0.68815	0.87097	1.02510	0.78573	0.89152	0.77481
Porosity II	0.1	0	1.82537	1.81580	1.81399	1.81882	1.81401	1.81627
		2	0.97917	1.14174	1.26335	1.06548	1.19361	1.10236
		10	0.81021	0.96686	1.10240	0.89042	1.01005	0.91828
	0.2	0	1.82690	1.80627	1.80240	1.81272	1.80249	1.80729
		2	0.92523	1.10286	1.23454	1.01967	1.15257	1.04963
		10	0.73873	0.91720	1.06670	0.83119	0.95332	0.84301
Porosity III	0.1	0	1.82629	1.83943	1.84445	1.83448	1.83928	1.83415
		2	1.02749	1.18429	1.30011	1.11116	1.24032	1.15545
		10	0.87183	1.01635	1.14240	0.94550	1.06821	0.98808
	0.2	0	1.82629	1.85285	1.86328	1.84275	1.85262	1.84215
		2	1.02749	1.19034	1.30929	1.11462	1.24874	1.16067
		10	0.87183	1.02002	1.14848	0.94733	1.07485	0.99248

The following formulations are used to estimate the non-dimensional deflections, stresses, natural frequencies and critical buckling loads of the FGSP with porosity

$$w^* = \frac{10hE_0}{a^2q_0}w\left(\frac{a}{2},\frac{b}{2}\right),\quad \sigma_x^* = \frac{10h^2}{a^2q_0}\sigma_x\left(\frac{a}{2},\frac{b}{2},\frac{h}{2}\right),\quad \tau_{xz}^* = \frac{h}{aq_0}\tau_x\left(0,\frac{b}{2},0\right)$$
$$\omega^* = \omega\frac{a^2}{h}\sqrt{\frac{\rho_0}{E_0}},\quad N_{cr}^* = N_{cr}\frac{a^2}{100h^3E_0},\quad E_0 = 1\ \text{GPa},\quad \rho_0 = 1\ \text{kg/m}^3,\quad h_0 = \frac{a}{10} \tag{65}$$

3.2.1. Static bending analysis of FGSP with porosity

For the static bending analysis, the FGSP is subjected to a sinusoidal distribution load with the maximum value of $q_0 = 1$. The non-dimensional center deflections, axial stress and transverse shear stress of the fully simple supported at all edges FGSP with $b/a = 1$, $a/h = 10$ are presented in Tables 11–13 for several values of power-law index and coefficient of porosity. It can be seen that the deflections and stresses of the plates do not depend on the schemes of the sandwich plates when $\xi = 0$, $p = 0$. In the general, the inclusion of the porosity effects leads to the rise of the deflections and stresses of the plates. The porosity III does not have effects on the behavior of (1-0-1) FGSP. The reason is that the (1-0-1) FGSP does not consist of the core layer.

Figs. 6 and 7 demonstrate the distribution of the axial and shear stresses through the thickness of the FGSP with different scheme and values of coefficient of porosity. It can see clearly that, although the scheme and distribution of porosity of the sandwich plates are symmetric, the distribution of the axial and shear stresses through the thickness of the FGSP are still asymmetric. It is due to the fact that the ingredients of two face sheets of the FGSP are different. These figures show that the scheme of the sandwich plate and the porosity affects strongly on the distribution of the axial and shear stresses. Figs. 6(b) and 7(b) show that the maximum values of the axial and shear stresses of the FGSP with porosity I are highest in comparison with other ones.

Fig. 8 demonstrates the effects of some parameters on the center deflections of the (1-1-1) FGSP with porosity. From Fig. 8(a), it is obvious that when the aspect ratio b/a increases, the center deflections of the plates increase. The increase rate of SSSS plates is greatest while the growing speed of CCCC ones is the smallest. It also sees that the center deflections of the CCCC plates and SCSC ones are similar when the aspect ratio greater than 2. The influence of the side-to-thickness ratio on the center deflections of the FGSP with porosity is exhibited in Fig. 8(b). The center deflections of the plates increase as the increase of the side-to-thickness ratio. Once again, the growing speed of the SSSS plates is greatest while the speed of the growing of CCCC ones is smallest. The influence of the power-law index p on the deflections of the FGSP is demonstrated in Fig. 8(c) while the effects of the porosity coefficient ξ on the center displacement of the FGSP are shown in Fig. 8(d). The deflections of the plates increase as the increase of the power-law index p and porosity coefficient ξ. From these two demonstrations, it is obvious that the effects of porosity III are much weaker than porosity I and porosity II, and the porosity I have significant effects on the behavior of the FGSP. In the case of porosity I, the center displacement of the (1-1-1) FGSP with $\xi = 0.2$ is approximately 1.3 times those without porosity.

3.2.2. Free vibration analysis of FGSP with porosity

Continuously, this subsection focusses on the analysis of free vibration of the square FGSP with porosity, and the side-to-thickness of $a/h = 10$. The non-dimensional fundamental frequency of the fully simple supported FGSP with porosity is given in Table 14. The non-dimensional first six frequencies of the FGSP with porosity subjected to different boundary conditions are demonstrated in Table 15.

Next, a (1-1-1) FGSP with porosity is considered here for the parameter study. The effects of the aspect ratio b/a and the side-to-

Table 15
The non-dimensional first six frequencies of square FGSP with porosity ($a/h = 10,\ p = 2,\ \xi = 0.2$).

Scheme	BCs	Porosity	Mode 1	Mode 2	Mode 3	Mode 4	Mode 5	Mode 6
1-1-1	CCCC	Perfect	2.06200	4.02117	4.02117	5.70096	6.81285	6.86932
		Porosity I	1.89447	3.72134	3.72134	5.30237	6.35735	6.40639
		Porosity II	1.94005	3.80145	3.80145	5.40735	6.47568	6.52692
		Porosity III	2.07935	4.04838	4.04838	5.73326	6.84616	6.90371
	SSCC	Perfect	1.58266	3.40719	3.42634	5.04513	5.44887	6.13301
		Porosity I	1.44808	3.13714	3.15390	4.66718	5.53734	5.68905
		Porosity II	1.48517	3.21073	3.22820	4.76924	5.48582	5.80790
		Porosity III	1.59736	3.43382	3.45332	5.07917	5.42278	6.17033
	SCSC	Perfect	1.67935	3.11078	3.82763	4.78258	5.10544	5.59335
		Porosity I	1.53940	2.85828	3.53821	4.72910	4.86228	5.16611
		Porosity II	1.57774	2.92754	3.61590	4.81582	4.83014	5.28254
		Porosity III	1.69428	3.13652	3.85439	4.76059	5.13856	5.63241
	SSSS	Perfect	1.17836	2.85498	2.85498	4.42924	4.78258	4.78258
		Porosity I	1.07373	2.61466	2.61466	4.07412	4.86228	4.86228
		Porosity II	1.10286	2.68124	2.68124	4.17204	4.81582	4.81582
		Porosity III	1.19034	2.88052	2.88052	4.46427	4.76059	4.76059
1-2-2	CCCC	Perfect	2.14671	4.16826	4.16826	5.89267	7.02727	7.08795
		Porosity I	2.02596	3.95654	3.95654	5.61484	6.71322	6.76821
		Porosity II	2.05412	4.00429	4.00429	5.67588	6.78051	6.83699
		Porosity III	2.15696	4.18279	4.18279	5.90832	7.04167	7.10310
	SSCC	Perfect	1.65155	3.54195	3.56242	5.23023	5.46857	6.34690
		Porosity I	1.55321	3.34777	3.36636	4.96158	5.56933	6.03370
		Porosity II	1.57671	3.39325	3.41233	5.02346	5.51289	6.10481
		Porosity III	1.66061	3.55733	3.57805	5.24867	5.43978	6.36604
	SCSC	Perfect	1.75058	3.23783	3.97004	4.80030	5.28901	5.80271
		Porosity I	1.64897	3.05491	3.76491	4.89061	5.02271	5.49647
		Porosity II	1.67299	3.09829	3.81158	4.83997	5.08339	5.56836
		Porosity III	1.75961	3.25311	3.98457	4.77608	5.30657	5.82448
	SSSS	Perfect	1.23259	2.97698	2.97698	4.60630	4.80030	4.80030
		Porosity I	1.15512	2.80111	2.80111	4.34909	4.89061	4.89061
		Porosity II	1.17401	2.84360	2.84360	4.41066	4.83997	4.83997
		Porosity III	1.24024	2.99265	2.99265	4.62686	4.77608	4.77608
2-2-1	CCCC	Perfect	2.15648	4.20601	4.20601	5.96348	7.12715	7.18601
		Porosity I	1.96805	3.86815	3.86815	5.51392	6.61301	6.66363
		Porosity II	2.02770	3.97407	3.97407	5.65370	6.77162	6.82498
		Porosity III	2.18154	4.24718	4.24718	6.01447	7.18198	7.24224
	SSCC	Perfect	1.65505	3.56343	3.58344	5.27687	5.75025	6.41511
		Porosity I	1.50407	3.26019	3.27756	4.85229	5.84576	5.91627
		Porosity II	1.55219	3.35630	3.37455	4.98620	5.79041	6.07282
		Porosity III	1.67578	3.60222	3.62268	5.32795	5.72849	6.47248
	SCSC	Perfect	1.75622	3.25328	4.00350	5.04688	5.34009	5.85008
		Porosity I	1.59902	2.97008	3.67761	4.91691	5.13246	5.37144
		Porosity II	1.64898	3.06016	3.78005	5.04994	5.08281	5.52315
		Porosity III	1.77752	3.29026	4.04362	5.02894	5.39035	5.90788
	SSSS	Perfect	1.23215	2.98558	2.98558	4.63216	5.04688	5.04688
		Porosity I	1.11504	2.71656	2.71656	4.23465	5.13246	5.13246
		Porosity II	1.15257	2.80260	2.80260	4.36151	5.08281	5.08281
		Porosity III	1.24874	3.02161	3.02161	4.68264	5.02894	5.02894

thickness ratio a/h are demonstrated in Fig. 9(a and b) for four cases of the boundary conditions. The frequencies of the fully clamped sandwich plates are greatest while those of fully simple supported ones are smallest. When the aspect ratio b/a and the side-to-thickness ratio a/h rise, the frequencies of the plates decrease. Fig. 9(c) demonstrates the effects of the power-law index p on the frequencies of the FGSP with porosity. When the power-law index increase, the frequencies decrease. The effects of porosity on the free vibration of the FGSP are demonstrated in Fig. 9(d). From this figure, when the porous coefficient ξ increase, the frequencies of the FGSP with porosity I and porosity II decrease rapidly, while the frequencies of the FGSP with porosity III increase slowly. According to Fig. 9(c and d), it can be concluded that the porosity III has weak effects on the frequencies of the FGSP while the porosity I and II have strong effects on the frequencies of that ones.

Fig. 10 illustrates the first nine mode shapes of the FGSP with porosity II subjected to SSCC boundary condition. Because the boundary condition is asymmetric, the mode shapes of the plate are asymmetric.

3.2.3. Buckling analysis of FGSP with porosity

The buckling behavior of the FGSP with porosity is investigated in this subsection. The plate is subjected to biaxial compressive load. The non-dimensional critical buckling load of the fully simple supported (SSSS) FGSP with porosity and $b/a = 1,\ a/h = 10$ is given in Table 16. It can see clearly that the power-law index and the porosity have significant effects on the buckling behavior of the plates. On the other hand, the effects of the boundary conditions on the critical buckling loads of the sandwich plates with porosity are presented in Table 17, where $b/a = 1,\ a/h = 10$ and $p = 2$. The critical buckling loads of the CCCC plates are greater than other ones, and those of SSSS plates are smallest.

Continuously, a (1-1-1) FGSP with porosity is examined in this subsection. The effects of the aspect ratio b/a on the critical buckling loads of the FGSP with porosity II are illustrated in Fig. 11(a). The critical buckling loads decrease as the increase of b/a. Fig. 11(b) demonstrates the effects of the side-to-thickness ratio a/h on the critical buckling loads of the FGSP with porosity. It can be seen that the side-to-thickness ratio have significant effects on the critical buckling loads of the FGSP. When the ratio a/h increases, the critical

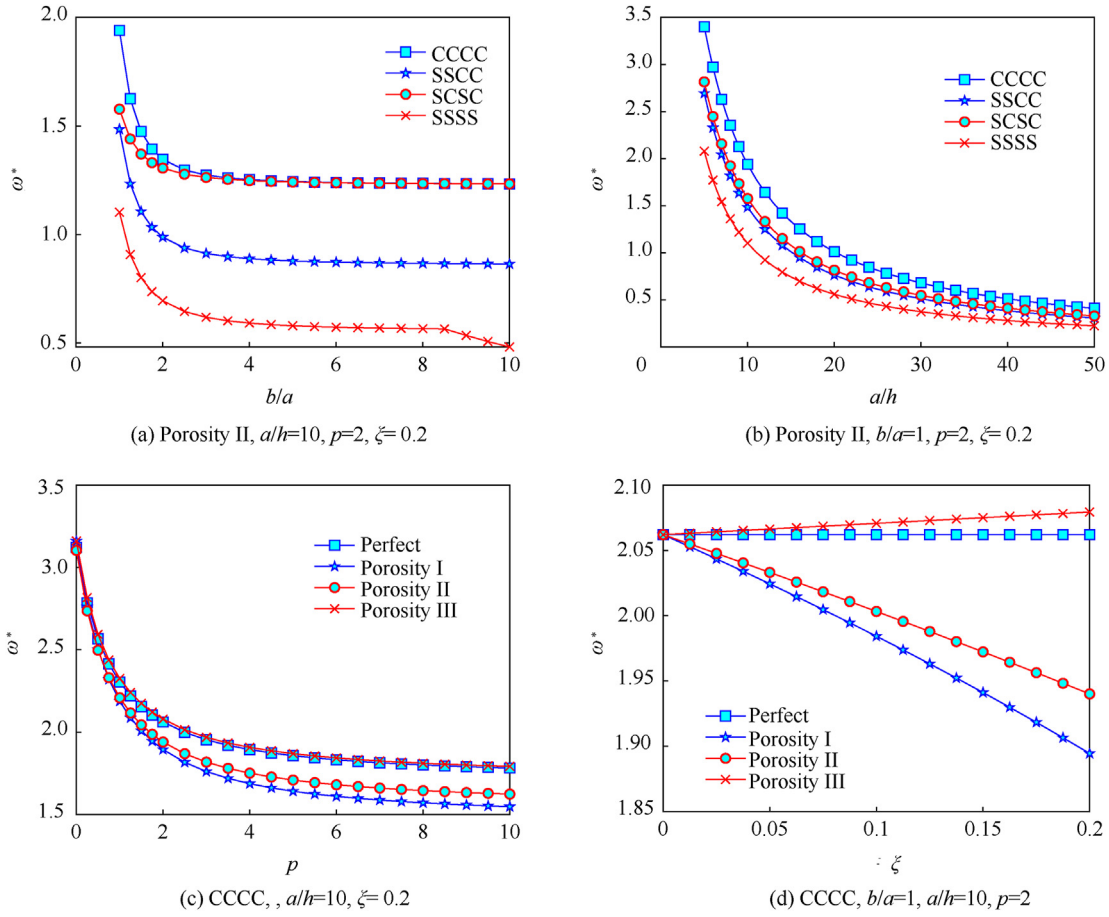

(a) Porosity II, a/h=10, p=2, ξ= 0.2

(b) Porosity II, b/a=1, p=2, ξ= 0.2

(c) CCCC, , a/h=10, ξ= 0.2

(d) CCCC, b/a=1, a/h=10, p=2

Fig. 9. The effects of several parameters on the center deflection of the (1-1-1) FGSP with porosity.

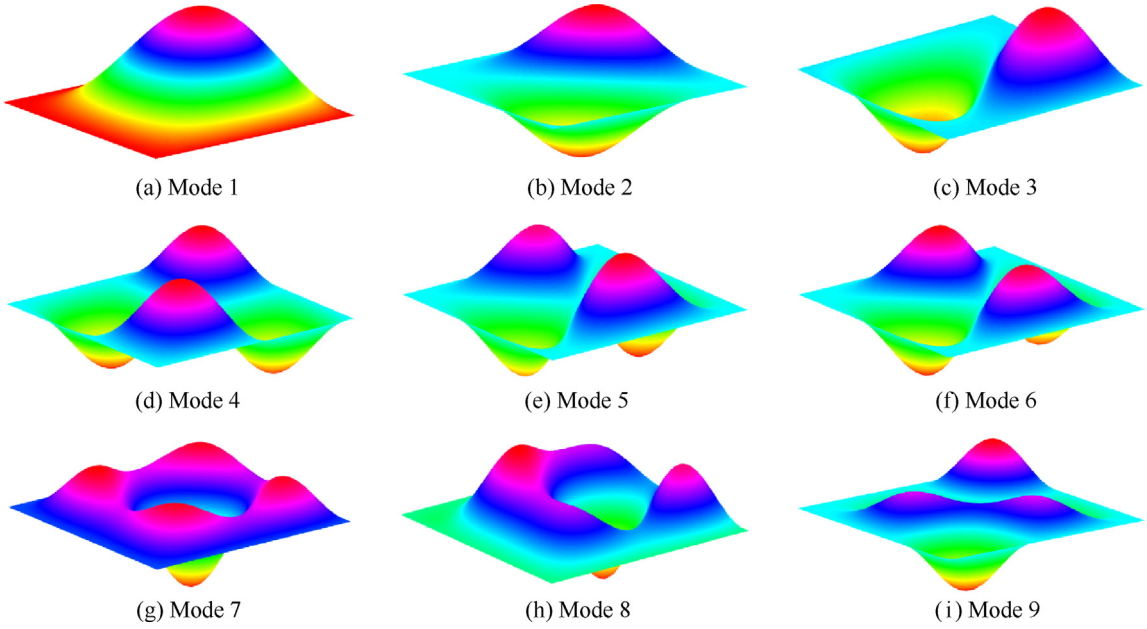

(a) Mode 1 (b) Mode 2 (c) Mode 3

(d) Mode 4 (e) Mode 5 (f) Mode 6

(g) Mode 7 (h) Mode 8 (i) Mode 9

Fig. 10. The first nine mode shapes of the SSCC (1-1-1) FGSP with porosity II ($b/a = 1,\ a/h = 10,\ p = 2,\ \xi = 0.2$).

Table 16
The non-dimensional critical buckling load of FGSP with porosity.

Porosity	ξ	p	1-0-1	1-1-1	1-2-1	2-1-2	2-2-1	2-1-1
Perfect	0	0	6.42089	6.42089	6.42089	6.42089	6.42089	6.42089
		2	2.61182	3.18582	3.67434	2.90372	3.14561	2.78886
		10	2.02711	2.48721	2.97462	2.24608	2.39359	2.10109
Porosity I	0.1	0	5.88466	5.91161	5.95985	5.89379	5.95731	5.92696
		2	2.13178	2.72602	3.25484	2.43094	2.69505	2.31005
		10	1.53277	2.03672	2.56585	1.77831	1.93411	1.60476
	0.2	0	5.37453	5.42669	5.52097	5.39203	5.51638	5.45761
		2	1.66787	2.28371	2.85165	1.97588	2.25786	1.84311
		10	1.04001	1.60178	2.17179	1.32512	1.48356	1.11122
Porosity II	0.1	0	6.02175	6.08679	6.13901	6.05554	6.12358	6.08658
		2	2.25903	2.88810	3.42246	2.57929	2.86008	2.46357
		10	1.67313	2.19336	2.72654	1.92479	2.10008	1.76265
	0.2	0	5.63842	5.76523	5.86754	5.70416	5.83742	5.76514
		2	1.91623	2.59881	3.17766	2.26408	2.58116	2.14492
		10	1.32640	1.90748	2.48525	1.61195	1.81204	1.42811
Porosity III	0.1	0	6.42089	6.40654	6.38753	6.41471	6.38377	6.39622
		2	2.61182	3.17349	3.64441	2.89824	3.12918	2.78234
		10	2.02711	2.47219	2.94319	2.23764	2.37940	2.09660
	0.2	0	6.42089	6.39173	6.35364	6.40827	6.34608	6.37142
		2	2.61182	3.16104	3.61450	2.89268	3.11273	2.77574
		10	2.02711	2.45698	2.91175	2.22909	2.36530	2.09206

Table 17
The non-dimensional critical buckling loads of FGSP with porosity with different BCs ($p = 2$).

Porosity	ξ	BCs	1-0-1	1-1-1	1-2-1	2-1-2	2-2-1	2-1-1
Perfect	0	CCCC	6.38735	7.79901	8.95384	7.11755	7.69654	6.83152
		SSCC	4.09094	4.99227	5.74513	4.55306	4.92833	4.37195
		SCSC	4.73633	5.78102	6.64460	5.27433	5.70663	5.06420
		SSSS	2.61182	3.18582	3.67434	2.90372	3.14561	2.78886
Porosity I	0.1	CCCC	5.24304	6.71249	7.97187	5.99483	6.63175	5.69464
		SSCC	3.34819	4.28374	5.10163	3.82281	4.23405	3.63247
		SCSC	3.88226	4.96816	5.90822	4.43546	4.91016	4.21481
		SSSS	2.13178	2.72602	3.25484	2.43094	2.69505	2.31005
	0.2	CCCC	4.12732	5.65627	7.01888	4.90297	5.58763	4.57356
		SSCC	2.62732	3.59872	4.48027	3.11643	3.55695	2.90746
		SCSC	3.05139	4.18008	5.19533	3.62178	4.13120	3.37953
		SSSS	1.66787	2.28371	2.85165	1.97588	2.25786	1.84311
Porosity II	0.1	CCCC	5.55396	7.09669	8.36394	6.35018	7.02267	6.06179
		SSCC	3.54740	4.53390	5.35869	4.05290	4.48866	3.87040
		SCSC	4.11280	5.25539	6.20232	4.70037	5.20242	4.48863
		SSSS	2.25903	2.88810	3.42246	2.57929	2.86008	2.46357
	0.2	CCCC	4.73659	6.40928	7.78730	5.59850	6.35981	5.30138
		SSCC	3.01688	4.08695	4.98208	3.56506	4.05773	3.37710
		SCSC	3.50269	4.74184	5.77061	4.13931	4.70730	3.92121
		SSSS	1.91623	2.59881	3.17766	2.26408	2.58116	2.14492
Porosity III	0.1	CCCC	6.38735	7.75945	8.86753	7.09817	7.64733	6.80987
		SSCC	4.09094	4.97008	5.69421	4.54265	4.89981	4.35997
		SCSC	4.73633	5.75350	6.58309	5.26112	5.67182	5.04920
		SSSS	2.61182	3.17349	3.64441	2.89824	3.12918	2.78234
	0.2	CCCC	6.38735	7.71881	8.77984	7.07822	7.59719	6.78761
		SSCC	4.09094	4.94746	5.64287	4.53200	4.87097	4.34774
		SCSC	4.73633	5.72532	6.52081	5.24756	5.63647	5.03381
		SSSS	2.61182	3.16104	3.61450	2.89268	3.11273	2.77574

buckling loads of the sandwich plates decrease rapidly. For SSSS plates, the critical buckling loads of the plate with $a/h = 50$ is approximately 20 times smaller than those of the plate with $a/h = 5$. The critical buckling loads of the CCCC plates with $a/h = 5$ is approximately 40 times greater than those of the plate with $a/h = 50$. Continuously, the influence of the power-law index p on the critical buckling loads of the FGSP with porosity is demonstrated in Fig. 11(c). The critical buckling loads of the plates decrease when p increases. The speeds of the decrease when the power-law index increases from 0 to 2 is greater than those of the plate when the power-law index increases from 2 to 10. Besides, it can see clearly that the effects of porosity III are very small in comparison with the effects of porosity I and porosity II. Fig. 11(d) presents the dependence of the critical buckling loads on the varying of the porous coefficient. In the general, the critical buckling loads of the porous plates are smaller than those of the perfect ones. The critical buckling loads of the plates with porosity I and porosity II decrease very fast when the porous coefficient ξ increases. However, the critical buckling loads of the plates with porosity III decrease slowly when the coefficient ξ increases. In general, the distribution of the porosities through the thickness of the plates plays a significant role on the buckling behavior of the FGSP with porosity.

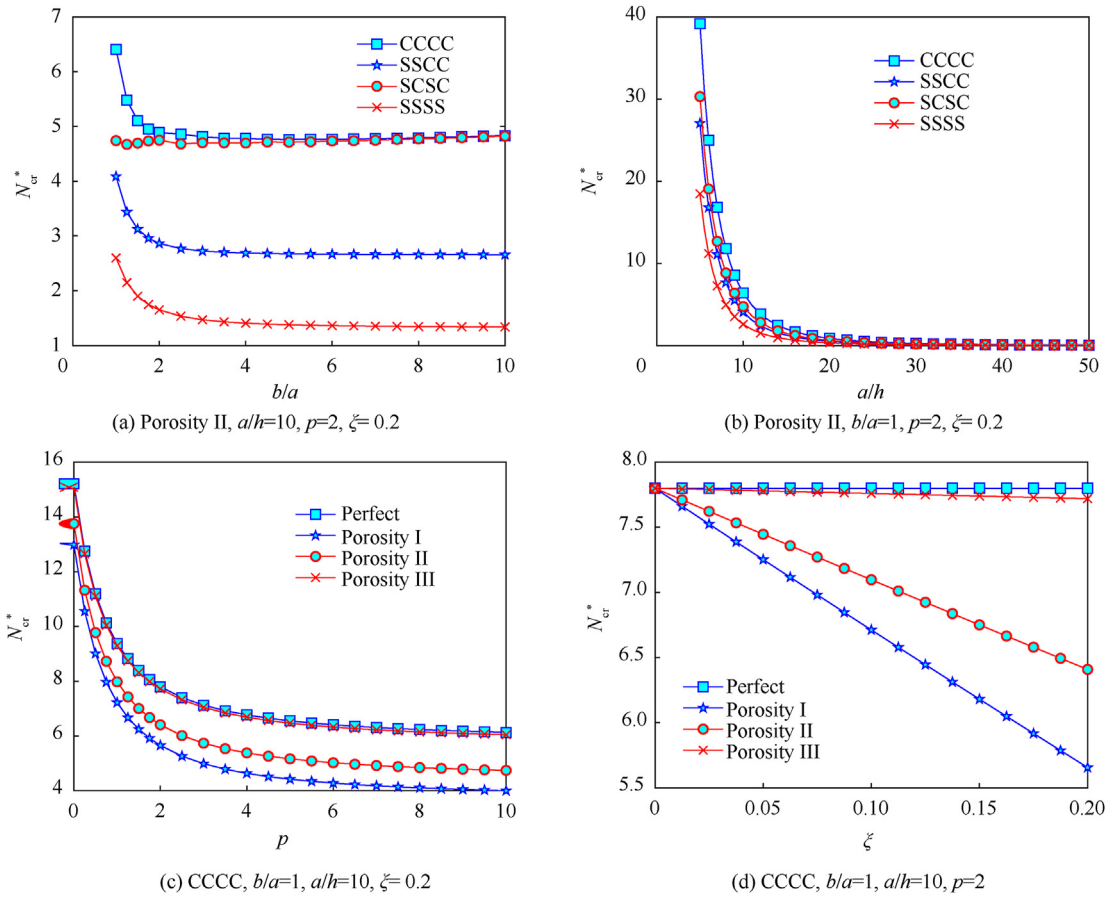

(a) Porosity II, a/h=10, p=2, ξ= 0.2

(b) Porosity II, b/a=1, p=2, ξ= 0.2

(c) CCCC, b/a=1, a/h=10, ξ= 0.2

(d) CCCC, b/a=1, a/h=10, p=2

Fig. 11. The effects of several parameters on the center deflection of the (1-1-1) FGSP with porosity.

4. Conclusions

In the conclusion of this study, a comprehensive study on the bending, free vibration and buckling analysis of the FGSP with porosity has been carried out. A finite element procedure based on a novel hyperbolic shear deformation theory has been established to predict the static and dynamic response of the FGSP with porosity. The accuracy and efficiency of the numerical results of the present algorithm are provided by comparing the present results and available results in some special cases. The present finite element algorithm can be applied to analyze the plates with arbitrary shape and boundary conditions. Some useful conclusions can be achieved as follows.

- The bending, free vibration and buckling behaviors of the FGSP are completely different from the conventional FGSP, especially the distribution of the stresses through the thickness of the plates.
- The inclusion of the porous effect leads to an increase of the deflections and critical buckling loads. However, the trend of the change in natural frequencies depends on the type of porous distribution.
- The location and distribution of the porosity affect strongly on the behavior of the FGSP. The porosity located at two face sheets has significant effects and the porosity located at core layer has small effects on the mechanical behavior of the FGSP.

The novel FGSP with porosity has a significant potential application in many fields of the aerospace, nuclear energy or marine engineering. So, it is necessary to have more works on the behavior of FGSP subjected to many types of loads such as thermal load, hygro-thermal load or blast pressure.

Funding

This research did not receive any specific grant from funding agencies in the public, commercial, or not-for-profit sectors.

Declaration of competing interest

The authors declare that they have no known competing financial interests or personal relationships that could have appeared to influence the work reported in this paper.

References

[1] Koizumi M. FGM activities in Japan. Compos B Eng 1997;28:1–4. https://doi.org/10.1016/S1359-8368(96)00016-9.
[2] Swaminathan K, Naveenkumar DT, Zenkour AM, Carrera E. Stress, vibration and buckling analyses of FGM plates - a state-of-the-art review. Compos Struct 2015;120:10–31. https://doi.org/10.1016/j.compstruct.2014.09.070.
[3] Thai HT, Kim SE. A review of theories for the modeling and analysis of functionally graded plates and shells. Compos Struct 2015;128(15):70–86. https://doi.org/10.1016/j.compstruct.2015.03.010.
[4] Nguyen HN, Tran TH, Vinh VP, Do VT. An efficient beam element based on quasi-3D theory for static bending analysis of functionally graded beams. Materials 2019;12(13):2198. https://doi.org/10.3390/ma12132198.
[5] Van TD, Van VP, Hoang NN. On the development of refined plate theory for static bending behavior of functionally graded plates. Math Probl Eng 2020: 2836763. https://doi.org/10.1155/2020/2836763.
[6] Reddy JN. Analysis of functionally graded plates. Int J Numer Methods Eng 2000;47:663–84. https://doi.org/10.1002/(SICI)1097-0207(20000110/30)47:1/3<663::AID-NME787>3.0.CO;2-8.
[7] Vu HN, Nam NH, Van-Vinh P, Khoa DN, Van-Thom D, Phung VM. A new

efficient modified first-order shear model for static bending and vibration behaviors of two-layer composite plate. Adv Civ Eng 2019:6814367. https://doi.org/10.1155/2019/6814367.
[8] Nguyen TK, Vo TP, Thai HT. Vibration and buckling analysis of functionally graded sandwich plates with improved transverse shear stiffness based on the first-order shear deformation theory. Proc IME C J Mech Eng Sci 2013;228(12):2110–31. https://doi.org/10.1177/0954406213516088.
[9] Nguyen HN, Tran TH, Pham VV, Nguyen DQ, Do VT. A refined simple first-order shear deformation theory for static bending and free vibration analysis of advanced composite plates. Materials;12(15):2385. https://doi.org/10.3390/ma12152385.
[10] Thai HT, Nguyen TK, Vo TP, Lee J. Analysis of functionally graded sandwich plates using a new first-order shear deformation theory. Eur J Mech Solid 2014;45:211–25. https://doi.org/10.1016/j.euromechsol.2013.12.008.
[11] Mantari JL, Granados EV. A refined FSDT for the static analysis of functionally graded sandwich plates. Thin-Walled Struct 2015;90:150–8. https://doi.org/10.1016/j.tws.2015.01.015.
[12] Zenkour AM. A comprehensive analysis of functionally graded sandwich plates: Part 1 Deflection and stresses. Int J Solid Struct 2005;42:5224–42. https://doi.org/10.1016/j.ijsolstr.2005.02.015.
[13] Zenkour AM. A comprehensive analysis of functionally graded sandwich plates: Part 2 - buckling and free vibration. Int J Solid Struct 2005;42:5243–58. https://doi.org/10.1016/j.ijsolstr.2005.02.016.
[14] Tounsi A, Houari MSA, Benyoucef S. A refined trigonometric shear deformation theory for thermoelastic bending of functionally graded sandwich plates. Aero Sci Technol 2013;24:209–20. https://doi.org/10.1016/j.ast.2011.11.009.
[15] Meksi R, Benyoucef S Mahmoudi A, Tounsi A, Adda Bedia EA, Mahmoud SR. An analytical solution for bending, buckling and vibration responses of FGM sandwich plates. J Sandw Struct Mater 2019;21(2):727–57. https://doi.org/10.1177/1099636217698443.
[16] Meziane MAA, Abdelaziz HH, Tounsi A. An efficient and simple refined theory for buckling and free vibration of exponentially graded sandwich plates under various boundary conditions. J Sandw Struct Mater 2014;16(3):293–318. https://doi.org/10.1177/1099636214526852.
[17] Bourada M, Tounsi A, Houari MSA, Bedia EAA. A new four-variable refined plate theory for thermal buckling analysis of functionally graded sandwich plates. J Sandw Struct Mater 2011;14(1):5–33. https://doi.org/10.1177/1099636211426386.
[18] Bennoun M, Houari MSA, Tounsi A. A novel five-variable refined plate theory for vibration analysis of functionally graded sandwich plates. Mech Adv Mater Struct 2016;23(4):423–31. https://doi.org/10.1080/15376494.2014.984088.
[19] Boukhatem F, Bessaim A, Kaci A, Mouffoki A, Houari MSA, Tounsi A, Heireche H, Bousahla AA. A novel refined plate theory for free vibration analysis of single-layered graphene sheets lying on Winkler-Pasternak elastic foundations. J Nano Res 2019;58:151–64. https://doi.org/10.4028/www.scientific.net/JNanoR.58.151.
[20] Meiche NE, Tounsi A, Ziane N, Mechab I, Bedia EAA. A new hyperbolic shear deformation theory for buckling and vibration of functionally graded sandwich plate. Int J Mech Sci 2011;53(4):237–47. https://doi.org/10.1016/j.ijmecsci.2011.01.004.
[21] Vinh PV, Dung NT, Tho NC, Thom DV, Le KH. Modified single variable shear deformation plate theory for free vibration analysis of rectangular FGM plates. Structure 2020;29:1435–44. https://doi.org/10.1016/j.istruc.2020.12.027.
[22] Hoa LK, Vinh PV, Duc ND, Trung NT, Son LT, Thom DV. Bending and free vibration analyses of functionally graded material nanoplates via a novel nonlocal single variable shear deformation plate theory. Proc IME C J Mech Eng Sci October 2020. https://doi.org/10.1177/0954406220964522.
[23] Li D, Deng Z, Xiao H. Thermomechanical bending analysis of functionally graded sandwich plates using four-variable refined plate theory. Compos B Eng 2016;106(1):107–19. https://doi.org/10.1016/j.compositesb.2016.08.041.
[24] Nguyen VH, Nguyen TK, Thai HT, Vo TP. A new inverse trigonometric shear deformation theory for isotropic and functionally graded sandwich plates. Compos B Eng 2014;66:233–46. https://doi.org/10.1016/j.compositesb.2014.05.012.
[25] Daikh AA, Zenkour AM. Effect of porosity on the bending analysis of various functionally graded sandwich plates. Mater Res Express 2019;6:065703. https://doi.org/10.1088/2053-1591/ab0971.
[26] Daikh AA, Zenkour AM. Free vibration and buckling of porous power-law and sigmoid functionally graded sandwich plates using a simple higher-order shear deformation theory. Mater Res Express 2019;6:115707. https://doi.org/10.1088/2053-1591/ab48a9.
[27] Daikh AA, Drai A, Houari MSA, Eltaher MA. Static analysis of multilayer nonlocal strain gradient nanobeam reinforced by carbon nanotubes. Steel Compos Struct 2020;36(6):643–56. https://doi.org/10.12989/SCS.2020.36.6.643.
[28] Sobhy. Size-dependent hygro-thermal buckling of porous FGM sandwich microplates and microbeams using a novel four-variable shear deformation theory. International Journal of Applied Mechanics 2020;12(2):2050017. https://doi.org/10.1142/S1758825120500179.
[29] Taj MG, Chakrabarti A, Talha M. Bending analysis of functionally graded skew sandwich plates with through-the thickness displacement variations. J Sandw Struct Mater 2014;16(2):210–48.
[30] Xuan HN, Thai CH, Thoi TN. Isogeometric finite element analysis of composite sandwich plates using a higher order shear deformation theory. Compos B Eng 2013;55:558–74. https://doi.org/10.1016/j.compositesb.2013.06.044.
[31] Daikh AA, Houari MSA, Eltaher MA. A novel nonlocal strain gradient Quasi-3D bending analysis of sigmoid functionally graded sandwich nanoplates. Compos Struct 2020;262:113347. https://doi.org/10.1016/j.compstruct.2020.113347.
[32] Neves AMA, Ferreira AJM, Carrera E, Cinefra M, Roque CMC, Jorge RMN, Soares CMM. Static, free vibration and buckling analysis of isotropic and sandwich functionally graded plates using a quasi-3D higher-order shear deformation theory and a meshless technique. Compos B Eng 2013;44:657–74. https://doi.org/10.1016/j.compositesb.2012.01.089.
[33] Neves AMA, Ferreira AJM, Carrera E, Cinefra M, Jorge RMN, Soares CMM. Buckling analysis of sandwich plates with functionally graded skins using a new quasi-3D hyperbolic sine shear deformation theory and collocation with radial basis functions. J Appl Math Mech 2012;92:749–66. https://doi.org/10.1002/zamm.201100186.
[34] Sobhy M, Radwan AF. A new quasi-3D nonlocal plate theory for vibration and buckling of FGM nanoplates. International Journal of Applied Mechanics 2017;9(1):1750008. https://doi.org/10.1142/S1758825117500089.
[35] Akavci SS. Mechanical behavior of functionally graded sandwich plates on elastic foundation. Compos B Eng 2016;96(1):136–52. https://doi.org/10.1016/j.compositesb.2016.04.035.
[36] Bessaim A, Houari MS, Tounsi A, Mahmoud S, Bedia EAA. A new higher-order shear and normal deformation theory for the static and free vibration analysis of sandwich plates with functionally graded isotropic face sheets. J Sandw Struct Mater 2013;15:671–703. https://doi.org/10.1177/1099636213498888.
[37] Zenkour AM. Bending analysis of functionally graded sandwich plates using a simple four-unknown shear and normal deformations theory. J Sandw Struct Mater 2013;15(6):629–56. https://doi.org/10.1177/1099636213498886.
[38] Iurlaro L, Gherlone M, Sciuva MD. Bending and free vibration analysis of functionally graded sandwich plates using the Refined Zigzag Theory. J Sandw Struct Mater 2014;16(6):669–99. https://doi.org/10.1177/1099636214548618.
[39] Neves AMA, Ferreira AJM, Carrera E, Cinefra M, Jorge RMN, Soares CMM. Static analysis of functionally graded sandwich plates according to a hyperbolic theory considering Zig-Zag and warping effects. Adv Eng Software 2012;52:30–43. https://doi.org/10.1016/j.advengsoft.2012.05.005.
[40] Dorduncu M. Stress analysis of sandwich plates with functionally graded cores using peridynamic differential operator and refined zigzag theory. Thin-Walled Struct 2020;146:106468. https://doi.org/10.1016/j.tws.2019.106468.
[41] Garg A, Chalak HD, Chakrabarti. Bending analysis of functionally graded sandwich plates using HOZT including transverse displacement effects. Mechanics based design of structures and machines. 2020. https://doi.org/10.1080/15397734.2020.1814157.
[42] Liu N, Jeffers AE. Isogeometric analysis of laminated composite and functionally graded sandwich plates based on a layerwise displacement theory. Compos Struct 2017;176(15):143–53. https://doi.org/10.1016/j.compstruct.2017.05.037.
[43] Pandey S, Pradyumna S. Free vibration of functionally graded sandwich plates in thermal environment using a layerwise theory. Eur J Mech Solid 2015;51:55–66. https://doi.org/10.1016/j.euromechsol.2014.12.001.
[44] Burlayenko VN, Sadowski T. Free vibrations and static analysis of functionally graded sandwich plates with three-dimensional finite elements. Meccanica 2020;55:815–32. https://doi.org/10.1007/s11012-019-01001-7.
[45] Vu HN, Pham VV, Nguyen VC, Do VT, Tran TH. A new beam model for simulation of the mechanical behaviour of variable thickness functionally graded material beams based on modified first order shear deformation theory. Materials 2019;12(3):404. https://doi.org/10.3390/ma12030404.
[46] Shahsavari D, Shahsavari M, Li L, Karami B. A novel quasi-3D hyperbolic theory for free vibration of FG plates with porosities resting on Winkler/Pasternak/Kerr foundation. Aero Sci Technol 2018;72:134–49. https://doi.org/10.1016/j.ast.2017.11.004.
[47] Zenkor AM. A quasi-3D refined theory for functionally graded single-layered and sandwich plates with porosities. Compos Struct 2018;201:38–48. https://doi.org/10.1016/j.compstruct.2018.05.147.
[48] Barati MR, Zenkour AM. Analysis of postbuckling of graded porous GPL-reinforced beams with geometrical imperfection. Mech Adv Mater Struct 2019;26(6):503–11. https://doi.org/10.1080/15376494.2017.1400622.
[49] Barati MR, Zenkour AM. Vibration analysis of functionally graded graphene platelet reinforced cylindrical shells with different porosity distributions. Mech Adv Mater Struct 2019;26(18):1580–8. https://doi.org/10.1080/15376494.2018.1444235.
[50] Sobhy M, Zenkour AM. Porosity and inhomogeneity effects on the buckling and vibration of double-FGM nanoplates via a quasi-3D refined theory. Compos Struct 2019;220:289–303. https://doi.org/10.1016/j.compstruct.2019.03.096.
[51] Zenkour AM, Aljadani MH. Porosity effect on thermal buckling behavior of actuated functionally graded piezoelectric nanoplates. Eur J Mech Solid 2019;78:103835. https://doi.org/10.1016/j.euromechsol.2019.103835.
[52] Zenkour AM. Quasi-3D refined theory for functionally graded porous plates: displacements and stresses. Phys Mesomech 2020;23:39–53. https://doi.org/10.1134/S1029959920010051.
[53] Mashat DS, Zenkour AM, Radwan AF. A quasi-3D higher-order plate theory for bending of FG plates resting on elastic foundations under hygro-thermo-mechanical loads with porosity. Eur J Mech Solid 2020;82:103985. https://doi.org/10.1016/j.euromechsol.2020.103985.